A century of reduced ENSO variability during the Medieval Climate Anomaly

A.E. Lawman[1,2]*, T.M. Quinn[1,2], J.W. Partin[1], K. Thirumalai[1,3], F.W. Taylor[1], C.-C. Wu[4,5], T.-.L Yu[4,5], M.K. Gorman[1,2], C.-C. Shen[4,5]

[1]Institute for Geophysics, Jackson School of Geosciences, The University of Texas at Austin, Austin, TX, USA, [2]Department of Geological Sciences, Jackson School of Geosciences, The University of Texas at Austin, Austin, TX, USA, [3]Department of Earth, Environmental and Planetary Sciences, Brown University – Providence, RI, USA, [4]High-precision Mass Spectrometry and Environment Change Laboratory (HISPEC), National Taiwan University, Taipei, Taiwan ROC, [5]Research Center for Future Earth, National Taiwan University, Taipei, Taiwan ROC

*Corresponding author: Allison Lawman (alawman@utexas.edu)

Key Points:

- Vanuatu coral Sr/Ca-SST variations are a proxy of El Niño-Southern Oscillation (ENSO) variability
- Vanuatu fossil coral Sr/Ca-SST variations indicate one hundred years of lower ENSO variability during part of the Medieval Climate Anomaly
- Periods of reduced ENSO variability can last a century, far longer than modern observations in the instrumental record of ENSO

1   **Abstract**

2   Climate model simulations of El Niño-Southern Oscillation (ENSO) behavior for the last
3   millennium demonstrate interdecadal to centennial changes in ENSO variability that can arise
4   purely from stochastic processes internal to the climate system. That said, the instrumental record
5   of ENSO does not have the temporal coverage needed to capture the full range of natural ENSO
6   variability observed in long, unforced climate model simulations. Here we demonstrate a
7   probabilistic framework to quantify changes in ENSO variability via histograms and probability
8   density functions using monthly instrumental and coral-based sea-surface temperature (SST)
9   anomalies from 1900-2005 CE and 1051-1150 CE. We find that reconstructed SST anomalies from
10   modern corals from the southwest Pacific capture changes in ENSO variability that are consistent
11   with instrumental SST data from the central equatorial Pacific. Fossil coral records indicate one
12   hundred years of relatively lower ENSO variability during part of the Medieval Climate Anomaly.
13   Our results demonstrate that periods of reduced ENSO variability can last a century, far longer in
14   duration than modern observations in the instrumental record of ENSO, but consistent with results
15   from unforced climate model simulations.

16   **Plain Language Summary**

17   The chemistry of coral skeletal material is a passive recorder of environmental conditions, like the
18   temperature of the water in which the coral lives. For example, the ratio of the element strontium
19   (Sr) to the element calcium (Ca) in the coral skeleton will vary in response to changes in sea surface
20   temperature (SST). Paleoclimatologists measure coral Sr/Ca to determine how SSTs vary in the
21   past. In this study, we use corals from the southwest Pacific to understand how SSTs in the tropical
22   Pacific Ocean varied during the 20th century and ~900 years ago during a time interval called the
23   Medieval Climate Anomaly. We focus on SST variability related to the El Niño-Southern
24   Oscillation (ENSO), a climate phenomenon that operates on year-to-year timescales and impacts
25   global temperature and rainfall patterns. Here we use temperature estimates inferred from corals
26   and find that past changes in ENSO variability during part of the Medieval Climate Anomaly is
27   similar to the early part of the 20th century.

28   **1 Introduction**

29   The El Niño-Southern Oscillation (ENSO) is a coupled ocean-atmosphere climate phenomenon
30   with global impacts on temperature and precipitation patterns [*Bjerknes*, 1969; *Ropelewski and*
31   *Halpert*, 1987]. ENSO is the leading mode of interannual (>1-9 year) climate variability, but
32   instrumental observations are of insufficient length [*Deser et al.*, 2010] to characterize the full
33   range of natural variability [*Wittenberg*, 2009]. Given the wide range of ENSO behavior simulated
34   in the absence of forcings external to the climate system [*Wittenberg*, 2009; *Deser et al.*, 2012], it
35   is critical to ascribe the degree to which anthropogenic warming and internal climate variability
36   are each contributing to future projections of ENSO in climate models [*Collins et al.*, 2010;
37   *DiNezio et al.*, 2013]. This motivates the use of paleo-ENSO reconstructions as out-of-sample tests
38   of climate model simulations [*Gagan et al.*, 2000; *Cobb et al.*, 2013; *Schmidt et al.*, 2014].
39
40   Isolating the unforced and forced components of ENSO variability remains an ongoing challenge
41   in paleoclimate science, particularly for different mean climate states when forcings were different
42   from today (e.g., the mid-Holocene or the Last Glacial Maximum) [*Masson-Delmotte et al.*, 2013;
43   *Liu et al.*, 2014]. Focusing on ENSO variability over the last two thousand years (the Common

44 Era, CE), provides context for the understanding of natural ENSO variability with current and
45 near-future climate change. The Medieval Climate Anomaly (MCA: 950-1250 CE [*Masson-*
46 *Delmotte et al.*, 2013]) is identified as an interval with Northern Hemisphere surface temperatures
47 similar to the modern [*Masson-Delmotte et al.*, 2013], but our understanding of paleo-ENSO
48 variability is inadequate due to a limited number of sub-annually resolved proxy records over the
49 last millennium [*Emile-Geay et al.*, 2013a; 2013b]. Furthermore, given that the magnitude of
50 orbital [*Bertrand et al.*, 2002], solar [*Bard et al.*, 2000], and volcanic [*Crowley*, 2000; *Gao et al.*,
51 2008] forcing during the MCA is both small and similar to the modern (pre-industrial), sustained
52 changes in ENSO variability are likely dominated by processes internal to the climate system
53 [*McGregor et al.*, 2013; *Rustic et al.*, 2015].
54
55 Coral records of surface ocean conditions extend our knowledge of interannual tropical climate
56 variability to places and times when there is no (or limited) instrumental data [*Fairbanks et al.*,
57 1997; *Gagan et al.*, 2000; *Corrège*, 2006]. Traditionally, coral-based ENSO reconstructions use
58 the standard deviation of a band-pass filtered time series (2-7 year window) of coral geochemical
59 proxies as a metric of past ENSO variability [*Cobb et al.*, 2003; 2013; *Hereid et al.*, 2013b; *Emile-*
60 *Geay et al.*, 2016], but this approach 1) filters out, by mathematical construction, important ENSO
61 variance that has a period of less than two years, and 2) necessitates many decades and longer
62 continuous datasets. Many fossil coral records, particularly older Holocene or Last Glacial
63 Maximum corals, are short (several decades or less) or discontinuous, and thus ill-suited for
64 traditional filtering and data analysis methods [*Tudhope*, 2001; *Cobb et al.*, 2013]. To address
65 these challenges, we extend the procedure suggested in *Trenberth* [1997] and use descriptive
66 statistics in tandem with probability theory by assessing histograms [*Trenberth*, 1997] and
67 probability density functions (PDFs) [*Parzen*, 1962] of monthly resolved coral data to quantify
68 changes in ENSO variability.
69
70 The Niño 3.4 SST index is a well-recognized record of ENSO variability [*Trenberth et al.*, 2002];
71 however, conditions in other regions of the tropical Pacific, notably the southwest Pacific, also
72 accurately record changes in ENSO variability [*Hereid et al.*, 2013a]. Departures from the long-
73 term monthly mean SST, (SST anomalies; SSTA) from the Niño 3.4 region (5°N-5°S, 120°-
74 170°W, Figure 1, box) in the central equatorial Pacific are canonically used to define the
75 occurrence of ENSO events [*Trenberth*, 1997]. During El Niño (La Niña) events, the central and
76 eastern tropical Pacific experience positive (negative) SST anomalies that peak during boreal
77 winter, while the western tropical Pacific experiences negative (positive) excursions [*Trenberth*,
78 1997] (Figure 1). Many paleo-ENSO studies target the Niño 3.4 region [*Cobb et al.*, 2003; *Nurhati*
79 *et al.*, 2009], but other regions of the Pacific, like the tropical southwest Pacific in the South Pacific
80 Convergence Zone, are also sensitive to ENSO variability, with ENSO detection skill broadly
81 similar to the Niño 3.4 region (60-70% skill) [*Hereid et al.*, 2013a]. The tropical southwest Pacific
82 is also advantageously home to abundant, high-quality modern and fossil corals, making this
83 region a suitable location for paleo-ENSO studies [*Quinn et al.*, 1996; *Linsley et al.*, 2006; *Quinn*
84 *et al.*, 2006; *Gorman et al.*, 2012; *Hereid et al.*, 2013b]. We also concentrate our efforts on
85 reconstructing decadal to interdecadal changes in paleo-ENSO variability, rather than
86 reconstructing the month-to-month changes of SST in the Niño 3.4 region, as this is difficult to
87 reconstruct back in time due to age uncertainties [*Emile-Geay et al.*, 2013a; 2013b].
88

89   Here we use modern corals from Vanuatu, an archipelago in the southwest Pacific (Figure 1, star),
90   to document ENSO variability during the 20th century, and fossil corals to determine ENSO
91   variability during the MCA. The recent decades of instrumental data (1982-2018) indicate that
92   71% of the variance of southwest Pacific SST anomalies is explained by ENSO. Despite the varied
93   amplitude of the SST response to different types of ENSO events [*Vincent et al.*, 2011; *Capotondi*
94   *et al.*, 2015], the southwest Pacific experiences a consistent SST response during ENSO events,
95   albeit of the opposite sign to the Niño 3.4 region (Figure S1): cooler SSTs during El Niño events
96   (Figure 1a) and warmer SSTs during La Niña events (Figure 1b). The consistent SST response at
97   Vanuatu during the most recent ENSO events increases our confidence in using coral records from
98   the tropical, southwest Pacific for paleo-ENSO studies. Fieldwork at Vanuatu identified and
99   recovered abundant, high-quality modern and fossil *Porites lutea* corals well-suited for ENSO
100   variability studies (Section 2.1). Due to the tectonic activity of south Pacific islands like Vanuatu
101   [*Taylor et al.*, 1987], the rate of uplift outpaces sea-level rise, which exposes fossil corals above
102   present day sea level. Another unique feature of our study site is that the fossil coral heads are all
103   *in situ* [*Thirumalai et al.*, 2015], allowing us to better understand the morphology of the reef flat,
104   and use estimates of the uplift rate to constrain the water depth in which the corals lived. We first
105   demonstrate our data analysis technique by quantifying instrumental SST variability in the Niño
106   3.4 region and then apply our methods to replicated coral Sr/Ca-SST records from the southwest
107   Pacific.

2 Materials and Methods

2.1 Coral Selection and Sampling

110   We located pristine, well-preserved, *in situ* fossil *P. lutea* coral heads spanning the last two
111   millennia from an uplifted reef offshore of Tasmaloum, Vanuatu (TMV: 15.6 °S, 166.9 °E). The
112   cores were drilled in 2011 using a Stihl chainsaw equipped with a Pomeroy Gear-Reduced Core
113   Drill and diamond coring bits. All coral cores were uranium-thorium (U-Th) dated at the High-
114   precision Mass Spectrometry and Environment Change Laboratory (HISPEC), National Taiwan
115   University, using multi-collector inductively coupled plasma mass spectrometry (MC-ICP-MS)
116   [*Shen et al.*, 2012; *Cheng et al.*, 2013]. Table S1 provides a summary of the properties for the
117   selected modern and fossil corals. Tables S2 and S3 provides the U-Th information for the ^{230}Th
118   age calculation. This study uses fossil corals 11-TM-S5 (^{230}Th ± 2σ age: 1127.1 ± 2.7 CE, 36.4 cm
119   depth) and 11-TM-I1 (^{230}Th ± 2σ ages: 1125.7 ± 6.2 CE, 30.5 cm depth; 1142.6 ± 4.9 CE, 18.0 cm
120   depth; 1149.0 ± 4.1 CE, 10.7 cm depth). Based on estimates of the uplift rate (~ 5.5 mm/year)
121   [*Taylor et al.*, 1990], the selected fossil coral heads grew approximately 1-3 m below the sea
122   surface during the Medieval Climate Anomaly.
123
124   To provide modern climatological context, the analysis incorporated core 06-SB-A1 collected
125   from a live *P. lutea* coral head at 8 m water depth at Sabine Bank, Vanuatu (SBV: 15.9 °S, 166.0
126   °E), ~90 km to the southwest of TMV. Core 06-SB-A1 was collected in 2006 using the French
127   Research Institute for Development (IRD) vessel R/V *Alis*. Core 06-SB-A1 has been previously
128   analyzed for oxygen isotopes [*Gorman et al.*, 2012], but this is the first study to present Sr/Ca data
129   from the same core. To quantify the replication uncertainty in our modern coral reconstructions,
130   we also incorporated 50 years (1941-1990 CE) of published modern coral Sr/Ca data from Malo
131   Channel, Vanuatu (MCV: 15.7 °S, 167.2 °E) [*Kilbourne et al.*, 2004].
132

133   X-ray images of 5 mm slabs extracted from the coral cores (Figure S2) highlighted the annual
134   density banding and the optimal sampling paths along the maximum growth axis. All slabs were
135   sonicated in distilled water and air dried prior to sampling. The coral slabs were micro-milled at
136   approximately monthly resolution (12 points/year) following established protocols [*Fairbanks and*
137   *Dodge*, 1979; *Alibert and McCulloch*, 1997; *Marshall and McCulloch*, 2002; *DeLong et al.*, 2013].
138   The sampling resolution varied from 0.5-1.0 mm depending on the average growth rate of each
139   respective coral (Table S1). The coral slabs were x-ray imaged a second time after micro-milling
140   (Figure S2) to confirm that the sampling paths were parallel to the growth direction of individual
141   corallites and along the central axis of a radially extending corallite fan [*DeLong et al.*, 2013].
142
143   To develop a reliable Sr/Ca-SST record, it is critical to ensure that the coral is sampled along the
144   maximum growth axis. We therefore considered how the coral growth architecture in three
145   dimensions is projected in the 2-D plane of the cross-sectional slabs. In the case of fossil coral 11-
146   TM-S5, we extracted additional 5 mm slabs from the core (Figure S2) to generate a continuous
147   record and ensure that the resultant Sr/Ca composite passed all of the quality control metrics
148   outlined in *DeLong et al.* [2013]. Sections with visible stress banding in the x-ray images and a
149   lack of clearly defined theca walls (e.g., the bottom of the 11-TM-I1 replication fossil coral;
150   Figures S2 and S4) are also sub-optimal as this can impact the annual cycle in the geochemistry
151   [*Marshall and McCulloch*, 2002] and/or make it difficult to identify the maximum growth axis for
152   sampling. Sub-optimal sampling can lead to unreliable climate reconstructions, so we excluded
153   sampling paths that did not pass the quality control metrics of *Delong et al.* [2013], and
154   conservatively limit our climate interpretations to the final Sr/Ca composites presented herein.

2.2 Coral Sr/Ca Analyses

156   Elemental ratio analyses were conducted using a Perkin Elmer Optima 8300 inductively coupled
157   plasma – optical emission spectrometer (ICP-OES) located at UT Austin. All Sr/Ca measurements
158   were corrected for plasma drift using standard-sample bracketing techniques [*Schrag*, 1999] with
159   an internal reference solution gravimetrically prepared to have Ca, Sr, and Mg proportions similar
160   to that of a coral. For each analysis, 113-262 µg of carbonate powder was dissolved in 2 wt. %
161   nitric acid such that the Ca^{2+} concentration in each sample was approximately 20 ppm, and within
162   our 8-32 ppm calibration range for Ca^{2+}.
163
164   The long-term precision of the Sr/Ca measurements for the 11-TM-S5, 11-TM-I1, and 06-SB-A1
165   samples is ±0.05% (2σ; 0.009 mmol/mol) based on repeated measurement (n > 7,500) of an
166   internal gravimetric standard, and ±0.06% (2σ; 0.012 mmol/mol) based on repeated measurement
167   (n > 800) of a homogenized coral powder from a *P. lutea* coral collected from Efate, Vanuatu
168   (17.7°S, 168.3°E) dissolved in 2 wt. % nitric acid. The analytical precision for the published MCV
169   Sr/Ca data is 0.15% (±2σ; 0.013 mmol/mol) based on 86 measurements of an in-house coral
170   standard [*Kilbourne et al.*, 2004].

2.3 Coral Sr/Ca Composites and Age Modeled Timeseries

172   X-ray images of the micro-milled coral slabs (Figure S2) provided clear constraints on the amount
173   of overlap between two sampling paths, and the strong seasonal cycle observed in coral Sr/Ca was
174   used to align peaks and troughs over the common period of overlap and generate the final Sr/Ca
175   composite records. For a given year in the coral time series, the highest Sr/Ca value indicates the
176   climatological coldest month, whereas the lowest Sr/Ca value indicates the climatological warmest

177　month. To convert Sr/Ca vs. depth to Sr/Ca vs. time, we used a MATLAB® algorithm to identify
178　the Sr/Ca peaks and troughs. The identified Sr/Ca maxima were assigned the climatological coldest
179　month at Vanuatu (August), and the Sr/Ca minima were assigned the climatological warmest
180　month (February). Once all of the annual peaks and troughs were identified, the Sr/Ca data was
181　linearly interpolated to achieve monthly resolution (12 points/year).
182
183　The relative age model for the modern SBV coral was converted to calendar years by counting
184　back from the date of collection, whereas the relative chronologies for the fossil corals were
185　converted to calendar years using four ^{230}Th ages as tie points (Tables S1-S3). The fossil coral
186　Sr/Ca time series were shifted within the analytical error (±2σ) of the four ^{230}Th ages (Figure S4)
187　such that the resulting overlap between 11-TM-S5 and 11-TM-I1 achieved the highest Pearson
188　correlation coefficient [*Pearson*, 1920] (r = 0.81, p < 0.01). We interpolated the published MCV
189　modern coral Sr/Ca [*Kilbourne et al.*, 2004] versus time data to 12 points/year using a piecewise
190　cubic hermite interpolating polynomial [*Fritsch and Carlson*, 1980]. We used a cubic interpolation
191　scheme as it better preserved the sinusoidal shape of the original MCV modern coral Sr/Ca data,
192　as compared to linear interpolation.

193　**3 Data Processing and Uncertainty Analysis**

194　**3.1 Instrumental Sea Surface Temperature (SST) Data**

195　All instrumental SST data is from the Met Office Hadley Centre 1° latitude x 1° longitude gridded
196　product (HadISST) [*Rayner et al.*, 2003]. SST data for the Niño 3.4 region was averaged over the
197　(5°S-5°N, 120°-170°W) domain (Figure 1 box). The 20th century historical ENSO events are based
198　on　　　　　the　　　　　Oceanic　　　　　Niño　　　　　Index　　　　　(NOAA:
199　http://origin.cpc.ncep.noaa.gov/products/analysis_monitoring/ensostuff/ONI_v5.php)　and　the
200　multi-variate ENSO index [*Wolter and Timlin*, 2011]. For Vanuatu, we computed an unweighted
201　average of the SST data from the two nearest grid points to the coral sites (15.5°S, 166.5°E) and
202　(16.5°S, 166.5°E). The average of the two SST series yielded a resulting SST series that better
203　represented the SST annual cycle observed in 7.75 years (Nov. 1999 - July 2007) of *in situ* SST
204　logger data from Sabine Bank, Vanuatu [*Ballu et al.*, 2013], as compared to using only a single
205　HadISST grid point for Vanuatu.

206　**3.2 Proxy Calibration (Sr/Ca-SST)**

207　We used the modern SBV coral Sr/Ca composite and gridded SST for Vanuatu to perform a
208　calibration-verification exercise [*Quinn and Sampson*, 2002] (Figure S3). We applied the
209　following linear calibration to all age-modeled modern and fossil coral Sr/Ca measurements: SST
210　(°C) = -20.73 x Coral Sr/Ca (mmol/mol) + 210.53. We also provide the inverse of the calibration
211　equation to facilitate comparison with other coral geochemical studies: Coral Sr/Ca (mmol/mol) =
212　-0.05 x SST (°C) + 10.16. To determine this calibration equation, we performed a weighted
213　bivariate regression [*Thirumalai et al.*, 2011] of the SST annual cycle (defined as the maximum
214　SST − minimum SST) vs. the SBV coral Sr/Ca annual cycle over the 1985-2005 CE calibration
215　window. We performed a regression using the annual cycle to minimize age uncertainty on the
216　monthly timescale. Although monthly resolution was targeted when sampling (Section 2.1), one
217　sample of coral powder may average 2-3 weeks (-2σ) of time when the coral is growing faster, or
218　5-6 weeks (+2σ) when the coral is growing slower. This yields some uncertainty in every
219　"monthly" Sr/Ca value. A month-to-month calibration with instrumental SST would incorporate

220 some of these errors. For this reason, we instead perform a regression using the annual cycle
221 because we are most confident in identifying the clear peaks and troughs in the Sr/Ca data. This
222 practice thus minimizes age uncertainty on the monthly timescale. When performing the weighted,
223 bivariate regression, we conservatively used 0.1 °C as the uncertainty in the instrumental SST, and
224 the analytical uncertainty (0.012 mmol/mol, $\pm 2\sigma$) as the uncertainty in coral Sr/Ca. The regression
225 was force fit through the origin to yield a slope value of -20.73 °C/mmol/mol. The y-intercept for
226 the calibration equation was empirically determined such that the median coral Sr/Ca-SST equaled
227 the median instrumental SST over the calibration interval.
228
229 We used 1985-2005 CE as the calibration interval because this window includes the most recent
230 20-years of modern coral data that overlaps with the most reliable subset of the instrumental record
231 that incorporates satellite observations [*Rayner et al.*, 2003]. The 1985-2005 CE calibration
232 window maximized the correlation with instrumental SST (r = 0.87, p < 0.01) and also minimized
233 the residual sum of squares over a 30-year verification window (1955 – 1984 CE) as compared to
234 other possible calibration intervals. We note that 4 other potential calibration intervals (1950-2005
235 CE, 1971-2000 CE, 1980-2005, 1985-2004 CE) yielded similar slope values (range: -19.55 to -
236 21.67 °C/mmol/mol) that were all within the range of published coral Sr/Ca-SST calibrations
237 [*Corrège*, 2006; *DeLong et al.*, 2010]. The coral trend of 0.83 °C/50 years at Sabine Bank (Figure
238 4a) resembles the trend of 0.5-0.75°C/50 years seen in observations for the southwest Pacific
239 [*Cravatte et al.*, 2009].

3.3 SST Data Processing

241 This subsection describes a series of mathematical operations that are used to isolate variability at
242 interannual (>1-9-year) timescales, the result of which preserves more variance than a 2-8-year
243 band-pass filter. We first applied a 9-year high-pass filter to the monthly instrumental and monthly
244 coral-based SST to remove decadal and longer variability. We then removed the climatology to
245 generate monthly SST anomalies calculated as deviations from the 1961-1990 CE climatology for
246 the tropical Pacific composite map (Figure 1), the Niño 3.4 and Vanuatu instrumental SST, and
247 the modern coral Sr/Ca-SST. Monthly SSTA were calculated as deviations from the 1126-1145
248 CE climatology for the MCA fossil corals. The climatology reference intervals were selected to
249 maximize the temporal overlap between contemporaneous records. Lastly, we computed a 5-
250 month running mean of monthly SSTA to smooth out intraseasonal variations [*Trenberth*, 1997].
251 All probability density function estimates (PDFs) of the monthly SST and monthly SSTA data
252 were computed using a kernel density estimation method [*Parzen*, 1962]. All instrumental and
253 coral-based monthly SST anomaly results are reported as 9-year high-pass filtered, climatology
254 removed, and 5-month running mean SSTA.

3.4 Uncertainty Analysis

256 We quantify changes in variability using the extreme percentiles ($p_{2.5}$ and $p_{97.5}$) of monthly SST
257 and SSTA distributions (Sections 5.1 and 5.2). We performed a Monte Carlo simulation (n =
258 10,000) to quantify the analytical and calibration uncertainties [*Thirumalai et al.*, 2014] in the 2.5
259 ($p_{2.5}$) and 97.5 ($p_{97.5}$) percentiles for the coral-based monthly SST and monthly SSTA distributions.
260 We also used replicated coral Sr/Ca records, to incorporate the effects of "geological" uncertainty,
261 which is due to all other sources including the oceanographic setting, sampling, etc. To calculate
262 the uncertainties in the extreme percentiles, we first subset all contemporaneous coral Sr/Ca
263 records to their common period of overlap prior to performing the Monte Carlo simulation

264 (Modern coral overlap: 1941-1990 CE; Fossil coral overlap: 1126-1145 CE). As part of the Monte
265 Carlo simulation, we perturbed each Sr/Ca data point in the original 50 (modern) or 20 (fossil)
266 year-long time series n times with values randomly sampled from a normal distribution with mean
267 zero and a standard deviation equal to the $\pm 2\sigma$ analytical uncertainty (± 0.012 mmol/mol). We then
268 transformed each Sr/Ca realization into SST taking uncertainty in the proxy calibration into
269 account. For each realization of the Sr/Ca time series, a slope value was randomly sampled from
270 a normal distribution centered on the empirically determined slope for Vanuatu (-20.73
271 °C/mmol/mol; Section 3.2) and a $\pm 2\sigma$ range that approximately spanned the range of published
272 coral Sr/Ca-SST calibration slopes [*Corrège*, 2006; *DeLong et al.*, 2010]. A corrective factor was
273 applied to the y-intercept such that the linear transformation for a given slope produced a y-
274 intercept that yielded the mean SST for the unperturbed time series. The resulting n SST
275 realizations generated for each modern and fossil coral record include the impact of both analytical
276 and calibration errors.

277
278 We next applied two filters to the coral records in order to remove long and short term variability
279 and isolate interannual variability. First, a 9-year high-pass filter was applied to the n SST
280 realizations prior to removing the climatology to remove variability on decadal and longer
281 timescales. The 5-month running mean of the climatology-removed SST anomaly series were then
282 computed to smooth out intraseasonal variations as defined in section 3.3 above. For each
283 realization of the SST and SSTA time series we computed the $p_{2.5}$ and $p_{97.5}$ values. The overall
284 uncertainty is the $\pm 2\sigma$ range based on n realizations. In the event that the $p_{2.5}$ and $p_{97.5}$ $\pm 2\sigma$ values
285 slightly differed for a given coral, we averaged the two values as the combined effect of analytical
286 and calibration uncertainty. The analytical and calibration uncertainty quantification for the
287 modern SBV coral is provided as an example (Figure S5).

288
289 We quantify the "geological" uncertainty in the coral records using replication. The total
290 uncertainties that include the effect of replication in the 2.5 and 97.5 percentiles of the SSTA
291 distributions are reported as the root mean square error of the percentile uncertainties for each
292 respective modern and fossil coral determined by the Monte Carlo simulation with analytical and
293 calibration uncertainty discussed above.

294
295 To test whether coral Sr/Ca-SSTA come from the same distribution, we performed Kolmogorov-
296 Smirnov (K-S) tests [*Massey*, 1951] at the 1% significance level. Given that the SSTA time series
297 are serially correlated, the effective degrees of freedom were considered when assessing the
298 significance [*Hu et al.*, 2017] of the K-S tests. Adjusting the effective degrees of freedom (ν_{eff})
299 makes it more difficult to reject the null hypothesis that the two datasets are from the same
300 distribution at a specified significance level. The statistical significance of the K-S tests is further
301 described and discussed in the results section. We also further explored the fidelity of the
302 differences in the $p_{2.5}$ and $p_{97.5}$ values taking the total uncertainty into account. We used the results
303 from our uncertainty analysis (e.g., Figure S5) to examine the overlap between the $p_{2.5}$ and $p_{97.5}$
304 distributions (additional details provided in sections 5.1 and 5.2 and Figures S6-S8).

305 **4. SST Variability in the Niño 3.4 Region**

306 We use instrumental SST data from the Niño 3.4 region [*Rayner et al.*, 2003] (Figure 2a) as a test-
307 case to demonstrate how a probabilistic framework quantifies previously identified changes in 20th
308 century ENSO variability [*Trenberth*, 1976; *Torrence and Compo*, 1998]. We choose a time-

309   domain subset of 1900-2005 CE to temporally match the modern coral climate record from
310   Vanuatu. Prior research has often quantified ENSO variability using power spectra [*Quinn et al.*,
311   1996; *Wittenberg*, 2009] and the standard deviation of band-pass filtered SSTA [*Cobb et al.*, 2003;
312   2013; *Emile-Geay et al.*, 2016]. In this study, we use an alternative statistical approach, involving
313   histograms and PDFs [*Trenberth*, 1997], which does not require continuous time series to
314   characterize changes in ENSO variability. Another advantage of using these techniques is that they
315   eliminate the need to identify discrete ENSO events, an ongoing challenge for paleo-ENSO records
316   due to dating uncertainties [*Emile-Geay et al.*, 2013b; *Hereid et al.*, 2013b; *Comboul et al.*, 2014].
317   Instead, we characterize variability based on the distribution of observations over a time interval,
318   an approach analogous to the analysis of individual foraminifera preserved in marine sediment
319   [*Thirumalai et al.*, 2013], albeit with more accurate annual chronology. The technique of looking
320   at changes in ENSO over windows in the past has also been previously employed using corals of
321   Holocene ages from the central Pacific [*Cobb et al.*, 2013].
322

323   The time series (Figure 2a) and histogram (Figure 2b) of Niño 3.4 monthly SST values [*Rayner et*
324   *al.*, 2003] include the total variability in the SST record, including annual, interannual, as well as
325   decadal and longer timescales. We note that for shorter records, linear or non-linear detrending
326   could be used in lieu of a high-pass filter to isolate interannual (sub-decadal) variability. SSTs in
327   the Niño 3.4 region document interdecadal variability in both the frequency and magnitude of
328   ENSO events during the instrumental record, with an increase of extreme events over the last 40
329   years [*Trenberth and Hoar*, 1996; *Cai et al.*, 2014; 2015]. For example, the 1982-83 and 1997-98
330   El Niño events (Figure 2c) are two out of the three most extreme ENSO events on record [*Santoso*
331   *et al.*, 2017]. We quantify changes in ENSO variability during the 20th century using two statistical
332   metrics computed in moving windows [*Okumura et al.*, 2017] (Figure 2e). Both the ± 2 standard
333   deviation range ($\pm 2\sigma$) (Figure 2e, dashed line) as well as the difference between the 2.5 ($p_{2.5}$) and
334   97.5 ($p_{97.5}$) percentiles (Figure 2e, solid line) show lower values during the early 20th century, and
335   higher values during the late 20th century that correspond with changes in the magnitude and/or
336   frequency of ENSO events, i.e. a change in ENSO variability. We note that if the data are normally
337   distributed (Gaussian), the $p_{2.5}$ to $p_{97.5}$ interpercentile range is approximately equal to the ± 2
338   standard deviation range.
339

340   These 20th century changes in ENSO variability observed in the time domain (Figure 2e) are also
341   captured using a probabilistic framework. We target intervals of enhanced and suppressed ENSO
342   variability [*Wittenberg*, 2009] as end-members to demonstrate that histogram width quantifies
343   changes in variability (Figure 2f). Extreme ENSO events yield SST anomalies that fall into the
344   tails of the SSTA distribution as defined by the 2.5 and 97.5 percentiles (Figure 2d). A change in
345   ENSO variability will correspondingly increase or decrease the $p_{2.5}$ to $p_{97.5}$ interpercentile range
346   (herein referred to as the width of the distribution). The increase in ENSO variability during the
347   late 20th century extends the overall width of the SSTA PDF (Figure 2f, red PDF) as compared to
348   the interval with less ENSO variability (Figure 2f, blue PDF). Although both negative (La Niña)
349   and positive (El Niño) SST anomalies become more extreme with increased ENSO variability, the
350   relative increase in El Niño-related positive SST anomalies is larger, corroborating documented
351   [*Trenberth*, 1997; *Cai et al.*, 2014; 2015] increases in the magnitude and frequency of strong El
352   Niño events during the late 20th century, i.e. an increase in skewness.
353

354 The distribution of SST anomalies from the Niño 3.4 region demonstrates that histograms and
355 PDFs quantify interdecadal changes in ENSO variability during the 20th century. Although we use
356 a continuous time series as demonstration, the histogram and PDF technique advantageously does
357 not require long and/or continuous climate records. We subsequently apply the same statistical
358 techniques to replicated SST records developed from modern and fossil corals from the tropical
359 southwest Pacific.

5 SST Variability in the Southwest Pacific (Vanuatu)

5.1 Modern SST Variability

362 While it is common practice to use instrumental observations to characterize modern SST
363 variability, observational coverage [*Deser et al.*, 2010] in the southwest Pacific is limited in the
364 first half of the 20th century (Figure 3a), which leads to uncertainty in the magnitude of changes in
365 ENSO-related SST variability. The SSTA signal in the observational product at Vanuatu (Figure
366 3d) is smaller compared to the Niño 3.4 region, but Vanuatu expectedly cools and warms during
367 known historical ENSO events (Figure S1, Figure 1, Figure 3d). However, instrumental SSTA at
368 Vanuatu does not document a clear difference in interdecadal ENSO variability (Figure 3f) as
369 observed in the Niño 3.4 region (Figure 2e). The PDF of instrumental monthly SSTA (Figure 3g)
370 for Vanuatu shows an increase in width during the late 20th century interval; however, the
371 difference between the more and less variable intervals is small and not statistically significant
372 (Section 3.4). The SSTA distributions (Figures 3e, 3g) have a large concentration of weak
373 anomalies, and the lack of interdecadal changes in ENSO variability is most likely due to the
374 statistical infilling of the climatological mean (i.e., zero-anomaly by construction in the data
375 product) SST when observations are lacking [*Reynolds and Smith*, 1994; *Rayner et al.*, 2003]
376 (Figure 3a). Care must be taken when interpreting the variability gridded SST products for data-
377 sparse regions, as interpolation, infilling, and other signal processing techniques lead to loss of
378 variance in these areas. Given a well-documented lack of variability in gridded SST products for
379 observation-limited regions [*Rayner et al.*, 2003], our modern coral-based SST reconstruction
380 augments limited SST products and demonstrates the need for additional modern coral climate
381 records from data-sparse regions.
382
383 The coral skeleton used to reconstruct and characterize modern monthly SST variability in the
384 southwest Pacific was collected from a live *P. lutea* coral head at 8 m water depth at Sabine Bank,
385 Vanuatu during a trip in 2006 [*Gorman et al.*, 2012] (15.9°S, 166.0°E; Section 2.1). We apply the
386 same analytical techniques used for instrumental SST to SST derived from coral Sr/Ca (Figure 4a)
387 to test how corals from the southwest Pacific record changes in ENSO variability.
388
389 The Sabine Bank modern coral Sr/Ca-SSTA reconstruction (Figure 4, Figure S3) faithfully
390 captures known interdecadal changes in ENSO variability over the last 100 years, as observed in
391 the Niño 3.4 region. The SSTA estimates from the corals (Figure 4c), which are a point source,
392 are larger than that for the spatially interpolated instrumental SST product (Figure 3d), which also
393 contains a known loss of variance [*Rayner et al.*, 2003]. More importantly, the coral reconstruction
394 agrees with the instrumental data that individual historical ENSO events alter SST in the region
395 (Figure 4c). Another notable distinction is that unlike instrumental SST, the SSTA reconstruction
396 from the coral archive faithfully captures known interdecadal changes in interannual variability
397 over the 20th century (Figure 4e). Reconstructed interannual SST variability at Vanuatu (Figure

398 4e) tracks the pattern of lower variability during the early 20th century and a late 20th century
399 increase in variability as observed in the Niño 3.4 region (Figure 2e). This change is also captured
400 by the PDFs for the select intervals with more and less ENSO variability (Figure 4f). La Niña-
401 related positive excursions become more extreme during the interval with enhanced ENSO
402 variability (Figure 4f; $p_{97.5}$ less variable/more variable: 0.63 vs. 1.00 °C). El Niño-related negative
403 SST anomalies also become more extreme ($p_{2.5}$ less variable/more variable: -0.83 vs. -1.26 °C).
404 The larger values for the variability metrics in moving windows (Figure 4e) in conjunction with
405 the increased width of the SSTA distribution for the interval with more ENSO variability (Figure
406 4f, red PDF) demonstrate that southwest Pacific modern coral Sr/Ca-SST captures the changes in
407 ENSO variability observed in instrumental SST for the Niño 3.4 region (Figure 2e, 2f).

409 Our uncertainty quantification explores whether the Sr/Ca estimates of SST result in larger changes
410 compared to instrumental data, and whether the changes in ENSO variability are statistically
411 significant. The reported uncertainty in the 2.5 and 97.5 percentiles for modern coral SSTA is
412 ±0.21 °C for the monthly SSTA (Figure 4d, 4f) based on a Monte Carlo error propagation
413 algorithm with analytical, calibration, and replication uncertainties [*Thirumalai et al.*, 2014]
414 (Figure S5, Section 3.4). Replication of the coral records quantifies the term that we refer to as
415 "geological" uncertainty, which is due to all other sources, including the oceanographic and
416 geologic setting, sampling, etc. We quantify this geological uncertainty by comparing two modern
417 corals over a common interval (1941-1990 CE) from the southwest Pacific (Section 3.4). Our
418 second, replication coral comes from Malo Channel, Vanuatu [*Kilbourne et al.*, 2004] (15.7°S,
419 167.2°E), ~120 km to the northeast of Sabine Bank.

421 The ±2σ range for the Sabine Bank modern coral SSTA distribution (1941-1990 replication
422 interval) is ±0.16 °C including analytical and calibration uncertainty (Figure S5). The ±2σ range
423 for the Malo Channel modern coral SSTA distribution (1941-1990 replication interval) is ±0.14
424 °C including analytical and calibration uncertainty. The resultant root mean square error is thus
425 ±0.21 °C as reported above. The modern coral SSTA distributions (Figure 6a) are reproducible
426 over their common period of overlap and come from the same continuous distribution (passes the
427 K-S test [*Massey*, 1951] at the 1% significance level regardless of the effective degrees of freedom;
428 Section 3.4). The intervals of more and less ENSO activity reconstructed from the Sabine Bank
429 modern coral SSTA (Figure 4f) are significantly different at an effective degree of freedom 65.8%
430 less (v_{eff} = 82) than the total number of months in each interval (n = 240; Section 3.4).

432 We further explored the fidelity of the differences in the $p_{2.5}$ and $p_{97.5}$ values taking the total
433 uncertainty into account. We used the results from our uncertainty analysis (Figure S5) to examine
434 the overlap between the $p_{2.5}$ and $p_{97.5}$ distributions for the intervals with more and less ENSO
435 variability (Figure S6). The amount of overlap between two percentile distributions highlights the
436 similarity or difference between the reported percentile values. Our analysis confirms that the
437 known changes in 20th century ENSO variability are recorded by corals from the southwest Pacific,
438 that the estimates are larger than instrumental estimates of SST changes, and that the changes in
439 ENSO variability are large compared to the calculated uncertainty of the coral-based SSTA
440 reconstruction.

441 **5.2 Medieval Climate Anomaly SST Variability**

442 After demonstrating that modern corals from the southwest Pacific capture observed changes in
443 ENSO variability, we next apply our statistical approach to corals from the MCA. The tectonic
444 activity at Tasmaloum, Vanuatu (15.6°S, 166.9°E) yields pristine, well-preserved *in situ* fossil
445 coral heads above present-day sea level. Our cores are collected from an uplifted reef, so we have
446 the unique opportunity to sample multiple, contemporaneous coral heads and quantify the
447 uncertainty in our fossil coral climate reconstruction via replication. The monthly SST anomalies
448 for both fossil corals are calculated with respect to the 1126-1145 CE climatology since this
449 interval is common to both corals. High precision U-Th dating [*Shen et al.*, 2012; *Cheng et al.*,
450 2013] confirms that the century-long fossil coral 11-TM-S5 (^{230}Th age: 1127.1 ± 2.7 CE, 2σ
451 analytical uncertainty) and the shorter, 24-year-long replication coral 11-TM-I1 (^{230}Th ages:
452 1125.7 ± 6.2, 1142.6 ± 4.9, 1149.0 ± 4.1 CE, 2σ analytical uncertainty) selected for this study were
453 alive ~900 years ago during the MCA (Section 2.1; Table S1).

455 We apply our statistical techniques to the SST record derived from fossil coral Sr/Ca (Figure 5a)
456 as a test of ENSO variability during a century of the MCA (1051–1150 CE). The MCA fossil coral
457 SST (Figure 5a) encompasses the total variability in the record (annual, interannual, as well as
458 decadal and longer timescales), and shows similar overall variability (Figure 5b) compared to the
459 modern period (Figure 4b). The SSTA time series (Figure 5c) shows both positive and negative
460 excursions that correspond to ENSO events. However, the number of large SSTA excursions is
461 smaller and leads to a narrower SSTA distribution (Figure 5d). While the modern SSTA shows a
462 unidirectional increase in ENSO variability from the early to late 20th century (Figure 4e),
463 interannual SST variability during the MCA fluctuates between intervals with more and less
464 variability (Figure 5e). For example, 1070-1090 CE has more interannual variability, while 1120-
465 1140 CE has less variability as quantified by the ±2σ and interpercentile ranges. However, neither
466 variability metric for the MCA (Figure 5e) exceeds the values for the last two decades of the 20th
467 century (Figure 4e).

469 We can compare the SSTA distribution for the MCA (Figure 5d) to either a century of modern
470 coral data (Figure 4d) or discrete windows of time in the modern era (Figure 4f). The values for
471 ENSO variability, as quantified by the percentiles of the SSTA distribution (Figure 5d), are 0.76
472 °C for La Niña-related SSTA ($p_{97.5}$) and -0.82 °C for El Niño-related SSTA ($p_{2.5}$), similar to what
473 we observe during the earlier part of the 20th century (Figure 4f). We choose to show an entire
474 century of data for the MCA, but note that our results are consistent if we choose a subset of the
475 fossil coral time series and generate the PDFs in 20-year moving windows (Figure S9).

477 The populations of SSTA for the two MCA fossil corals (Figure 6b) are drawn from the same
478 distribution over their common interval of overlap, as they pass the K-S test [*Massey*, 1951] at the
479 1% significance level (regardless of the effective degrees of freedom; Section 3.4). The uncertainty
480 in extreme monthly SSTA values (Figure 5d, 2.5 and 97.5 percentiles) is ±0.24 °C based on our
481 algorithm with analytical, calibration and geological uncertainty (Section 3.4). Incorporating the
482 total uncertainty, we find that ENSO variability during the MCA, as recorded by the fossil corals,
483 is within the range of ENSO variability observed in the modern and is significantly different than
484 the interval with more ENSO variability during the late 20th century (Figure S7). Moreover, we
485 cannot distinguish the SSTA population that records ENSO variability during the MCA as
486 significantly different than the modern interval with less ENSO variability (based on K-S tests
487 [*Massey*, 1951] at the 1% significance level and Figure S8). That said, we can distinguish the

488 SSTA population during the MCA as significantly different than the SSTA population during
489 modern interval with more ENSO variability (via the K-S test), and the new coral records from
490 Vanuatu show less ENSO variability during the MCA as compared to the late 20th century.

6 Discussion and Conclusions

492 Previously published proxy records of ENSO [*Moy et al.*, 2002; *Cobb et al.*, 2003; *Rein et al.*,
493 2004; *Newton et al.*, 2006; *Rustic et al.*, 2015] for the MCA and the Little Ice Age (LIA: 1450-
494 1850 CE [*Masson-Delmotte et al.*, 2013]) often show conflicting results, indicating large
495 uncertainties in the proxy records, in our estimations of the range of natural variability, or both.
496 Numerous records provide evidence for a strengthened SST gradient across the equatorial Pacific
497 and/or an inferred reduction in ENSO variability during the MCA relative to the LIA [*Cobb et al.*,
498 2003; *Newton et al.*, 2006; *Rustic et al.*, 2015]. In contrast, other proxy records [*Moy et al.*, 2002;
499 *Rein et al.*, 2004] indicate a peak in ENSO variability during the MCA. Two recent compilations
500 of ENSO-sensitive records actually find no statistically significant change in ENSO variability
501 between the MCA and the LIA and highlight the need for additional high-resolution proxy records
502 to fully characterize the range of ENSO variability over the Common Era [*Emile-Geay et al.*,
503 2013b; *Henke et al.*, 2017].

505 Internal climate variability contributes a large source of uncertainty in detecting forced changes in
506 ENSO variability over the Common Era. Our results show a prolonged period of low variability
507 during a time with external forcings similar to pre-industrial values [*Bradley et al.*, 2016]. We
508 interpret our results in tandem with the compilation studies to indicate that devoid of strong
509 external climate forcing, internal variability within the climate system can produce a wide range
510 of responses in the variability of ENSO. The PDF for coral data from the MCA indicates that
511 ENSO variability over a full century is statistically indistinguishable from two decades with less
512 ENSO variability observed during the 20th century (Figure 7, Figure S8). We show a century of
513 data for the MCA and 20 years of data for the modern, but our results are consistent if we choose
514 a subset of the fossil coral time series and generate the PDFs in 20-year moving windows (Figure
515 S9). Furthermore, even when including the total uncertainty in the coral reconstructions ($\pm 2\sigma$
516 analytical, calibration, and geological uncertainty), ENSO variability during the MCA and the
517 early 20th century is statistically different and lower than the recent decades with larger ENSO
518 variability (Figures S6 and S7). Thus, we conclude that while the MCA contained lower ENSO
519 variability, such ranges have been observed in the historical record.

521 Although our study focuses on ENSO variability during the Common Era, the histogram and PDF
522 technique we present here is broadly applicable to other paleoclimate studies that seek to
523 reconstruct variability across a variety of timescales. Quantifying the range of natural variability
524 is critical as it may complicate our ability to detect a forced ENSO response from short records
525 during times with different background states such as the mid-Holocene, the Last Glacial
526 Maximum, future climate scenarios, and the most recent decades of instrumental data. Only by
527 collecting more paleoclimate proxy data can we establish a baseline to determine if changes in
528 ENSO variability during these other times are outside the bounds of natural variability. Our
529 findings provide new insight to this challenge by replicating the bounds of low ENSO variability
530 from two different time periods, and showing that intervals of low ENSO variability can last for a
531 full century, consistent with multi-decadal to centennial intervals of reduced ENSO variability
532 simulated in unforced climate models [*Wittenberg*, 2009; *Deser et al.*, 2012].

Author Contributions

A.E.L wrote the manuscript, sampled the fossil corals, and performed all the fossil coral Sr/Ca analyses. A.E.L performed the data analysis and interpreted the results with T.M.Q and J.W.P. K.T. assisted with the data analysis and uncertainty quantification. F.W.T. drilled the modern coral, and F.W.T and J.W.P drilled the fossil coral samples with support from T.M.Q. M.K.G. sampled the modern coral from Sabine Bank, Vanuatu and generated the original modern coral Sr/Ca data composite. C.-C.S, C.-C.W, and T.-L.Y provided the ^{230}Th ages for the fossil corals. All authors reviewed the manuscript.

Data Availability

All coral Sr/Ca data from Sabine Bank and Tasmaloum, Vanuatu produced from this study is archived in the paleoclimatology dataset repository in the National Centers for Environmental Information, NOAA database: https://www.ncdc.noaa.gov/data-access/paleoclimatology-data/datasets/coral-sclerosponge.

Code Availability

The MATLAB® codes that have contributed to the analysis and results in this study are available upon request from the lead author (A.E.L: alawman@utexas.edu). The age model algorithm used to transform the coral geochemical data from the depth to the time domain is publicly available on the GitHub repository for the lead author: https://github.com/lawmana/coralPSM.

Additional Information

Supporting information is available for this paper.

 Competing Financial Interests: The authors declare no competing financial interests.

Correspondence and requests for materials should be addressed to A.E.L.

References

Alibert, C., and M. T. McCulloch (1997), Strontium/calcium ratios in modern *Porites* corals from the Great Barrier Reef as a proxy for sea surface temperature: Calibration of the thermometer and monitoring of ENSO, *Paleoceanography*, *12*(3), 345–363, doi:10.1029/97PA00318.

Ballu, V., P. Bonnefond, S. Calmant, M. N. Bouin, B. Pelletier, O. Laurain, W. C. Crawford, C. Baillard, and O. de Viron (2013), Using altimetry and seafloor pressure data to estimate vertical deformation offshore: Vanuatu case study, *Adv. Space Res.*, *51*(8), 1335–1351, doi:10.1016/j.asr.2012.06.009.

Bard, E., G. Raisbeck, F. Yiou, and J. Jouzel (2000), Solar irradiance during the last 1200 years based on cosmogenic nuclides, *Tellus*, *52B*, 985–992, doi:10.3402/tellusb.v52i3.17080.

Bertrand, C., M. F. Loutre, M. Crucifix, and A. Berger (2002), Climate of the last millennium: A sensitivity study, *Paleoceanography*, *52A*, 221–244, doi:10.1034/j.1600-0870.2002.00287.x.

Bjerknes, J. (1969), Atmospheric teleconnections from the equatorial pacific, *Mon. Weather Rev.*, *97*(3), 163–172, doi:10.1175/1520-0493(1969)097<0163:ATFTEP>2.3.CO;2.

Bradley, R. S., H. Wanner, and H. F. Diaz (2016), The Medieval Quiet Period, *The Holocene*, *26*(6), 990–993, doi:10.1177/0959683615622552.

Cai, W. et al. (2014), Increasing frequency of extreme El Niño events due to greenhouse warming, *Nature Climate Change*, *4*(2), 111–116, doi:10.1038/nclimate2100.

Cai, W. et al. (2015), Increased frequency of extreme La Niña events under greenhouse warming, *Nature Climate Change*, *5*(2), 132–137, doi:10.1038/nclimate2492.

Capotondi, A. et al. (2015), Understanding ENSO Diversity, *Bull. Amer. Meteor. Soc.*, *96*(6), 921–938, doi:10.1175/BAMS-D-13-00117.1.

Cheng, H. et al. (2013), Improvements in ^{230}Th dating, ^{230}Th and ^{234}U half-life values, and U–Th isotopic measurements by multi-collector inductively coupled plasma mass spectrometry, *Earth Planet. Sci. Lett.*, *371-372*(C), 82–91, doi:10.1016/j.epsl.2013.04.006.

Cobb, K. M., C. D. Charles, H. Cheng, and R. E. Nature (2003), El Niño/Southern Oscillation and tropical Pacific climate during the last millennium, *Nature*, *424*(6946), 271–276, doi:10.1038/nature01779.

Cobb, K. M., N. Westphal, H. R. Sayani, J. T. Watson, E. Di Lorenzo, H. Cheng, R. L. Edwards, and C. D. Charles (2013), Highly variable El Niño–Southern Oscillation throughout the Holocene, *Science*, *339*(6115), 67–70, doi:10.1126/science.1228246.

Collins, M. et al. (2010), The impact of global warming on the tropical Pacific Ocean and El Niño, *Nature Geosci.*, *3*(6), 391–397, doi:10.1038/ngeo868.

606 Comboul, M., J. Emile-Geay, M. N. Evans, N. Mirnateghi, K. M. Cobb, and D. M. Thompson
607   (2014), A probabilistic model of chronological errors in layer-counted climate proxies:
608   applications to annually banded coral archives, *Clim. Past*, *10*(2), 825–841, doi:10.5194/cp-
609   10-825-2014.

610 Corrège, T. (2006), Sea surface temperature and salinity reconstruction from coral geochemical
611   tracers, *Palaeogeogr. Palaeoclimatol. Palaeoecol.*, *232*(2-4), 408–428,
612   doi:10.1016/j.palaeo.2005.10.014.

613 Cravatte, S., T. Delcroix, D. Zhang, M. McPhaden, and J. Leloup (2009), Observed freshening
614   and warming of the western Pacific Warm Pool, *Clim Dyn*, *33*(4), 565–589,
615   doi:10.1007/s00382-009-0526-7.

616 Crowley, T. J. (2000), Causes of climate change over the past 1000 Years, *Science*, *289*(5477),
617   270–277, doi:10.1126/science.289.5477.270.

618 DeLong, K. L., T. M. Quinn, C.-C. Shen, and K. Lin (2010), A snapshot of climate variability at
619   Tahiti at 9.5 ka using a fossil coral from IODP Expedition 310, *Geochem. Geophys.
620   Geosyst.*, *11*(6), doi:10.1029/2009GC002758.

621 DeLong, K. L., T. M. Quinn, F. W. Taylor, C.-C. Shen, and K. Lin (2013), Improving coral-base
622   paleoclimate reconstructions by replicating 350 years of coral Sr/Ca variations, *Palaeogeogr.
623   Palaeoclimatol. Palaeoecol.*, *373*(C), 6–24, doi:10.1016/j.palaeo.2012.08.019.

624 Deser, C., A. S. Phillips, R. A. Tomas, Y. Okumura, M. A. Alexander, A. Capotondi, J. D. Scott,
625   Y.-O. Kwon, and M. Ohba (2012), ENSO and Pacific decadal variability in the Community
626   Climate System Model version 4, *J. Clim.*, *25*, 2622–2651, doi:10.1175/JCLI-D-11-00301.1.

627 Deser, C., M. A. Alexander, S.-P. Xie, and A. S. Phillips (2010), Sea surface temperature
628   variability: Patterns and mechanisms, *Annu. Rev. Marine. Sci.*, *2*(1), 115–143,
629   doi:10.1146/annurev-marine-120408-151453.

630 DiNezio, P. N., G. A. Vecchi, and A. C. Clement (2013), Detectability of changes in the Walker
631   circulation in response to global warming, *J. Climate*, *26*(12), 4038–4048, doi:10.1175/JCLI-
632   D-12-00531.1.

633 Emile-Geay, J. et al. (2016), Links between tropical Pacific seasonal, interannual and orbital
634   variability during the Holocene, *Nature Geosci.*, *9*(2), 168–173, doi:10.1038/ngeo2608.

635 Emile-Geay, J., K. M. Cobb, M. E. Mann, and A. T. Wittenberg (2013a), Estimating central
636   equatorial Pacific SST variability over the past millennium. Part I: Methodology and
637   validation, *J. Climate*, *26*(7), 2302–2328, doi:10.1175/JCLI-D-11-00510.1.

638 Emile-Geay, J., K. M. Cobb, M. E. Mann, and A. T. Wittenberg (2013b), Estimating central
639   equatorial Pacific SST variability over the past millennium. Part II: Reconstructions and
640   implications, *J. Climate*, *26*(7), 2329–2352, doi:10.1175/JCLI-D-11-00511.1.

641   Fairbanks, R. G., and R. E. Dodge (1979), Annual periodicity of the and ratios in the coral
642   Montastrea annularis, *Geochim. Cosmochim. Acta*, *43*(7), 1009–1020, doi:10.1016/0016-
643   7037(79)90090-5.

644   Fairbanks, R. G., M. N. Evans, J. L. Rubenstone, R. A. Mortlock, K. Broad, M. D. Moore, and
645   C. D. Charles (1997), Evaluating climate indices and their geochemical proxies measured in
646   corals, *Coral Reefs*, *16*(1), S93–S100, doi:10.1007/s003380050245.

647   Fritsch, F. N., and R. E. Carlson (1980), Monotone piecewise cubic interpolation, *SIAM*, *17*(2),
648   238–246, doi:10.1137/0717021.

649   Gagan, M. K., L. K. Ayliffe, J. W. Beck, J. E. Cole, E. Druffel, R. B. Dunbar, and D. P. Schrag
650   (2000), New views of tropical paleoclimates from corals, *Quat. Sci. Rev.*, *19*, 45–64,
651   doi:10.1016/S0277-3791(99)00054-2.

652   Gao, C., A. Robock, and C. Ammann (2008), Volcanic forcing of climate over the past 1500
653   years: An improved ice core-based index for climate models, *J. Geophys. Res.*, *113*(D23),
654   D23111–15, doi:10.1029/2008JD010239.

655   Gorman, M. K., T. M. Quinn, F. W. Taylor, J. W. Partin, G. Cabioch, J. A. Austin Jr., B.
656   Pelletier, V. Ballu, C. Maes, and S. Saustrup (2012), A coral-based reconstruction of sea
657   surface salinity at Sabine Bank, Vanuatu from 1842 to 2007 CE, *Paleoceanography*, *27*(3),
658   doi:10.1029/2012PA002302.

659   Henke, L. M. K., F. H. Lambert, and D. J. Charman (2017), Was the Little Ice Age more or less
660   El Niño-like than the Medieval Climate Anomaly? Evidence from hydrological and
661   temperature proxy data, *Clim. Past*, *13*(3), 267–301, doi:10.5194/cp-13-267-2017.

662   Hereid, K. A., T. M. Quinn, and Y. M. Okumura (2013a), Assessing spatial variability in El
663   Niño-Southern Oscillation event detection skill using coral geochemistry,
664   *Paleoceanography*, *28*(1), 14–23, doi:10.1029/2012PA002352.

665   Hereid, K. A., T. M. Quinn, F. W. Taylor, C. C. Shen, R. Lawrence Edwards, and H. Cheng
666   (2013b), Coral record of reduced El Nino activity in the early 15th to middle 17th centuries,
667   *Geology*, *41*(1), 51–54, doi:10.1130/G33510.1.

668   Hu, J., J. Emile-Geay, and J. Partin (2017), Correlation-based interpretations of paleoclimate
669   data – where statistics meet past climates, *Earth Planet. Sci. Lett.*, *459*, 362–371,
670   doi:10.1016/j.epsl.2016.11.048.

671   Kennedy, J. J., N. A. Rayner, R. O. Smith, D. E. Parker, and M. Saunby (2011a), Reassessing
672   biases and other uncertainties in sea surface temperature observations measured in situ since
673   1850: 1. Measurement and sampling uncertainties, *J. Geophys. Res.*, *116*(D14), D12106–13,
674   doi:10.1029/2010JD015218.

675   Kennedy, J. J., N. A. Rayner, R. O. Smith, D. E. Parker, and M. Saunby (2011b), Reassessing
676   biases and other uncertainties in sea surface temperature observations measured in situ since

677 1850: 2. Biases and homogenization, *J. Geophys. Res.*, *116*(D14), 1–22,
678 doi:10.1029/2010JD015220.

679 Kilbourne, K. H., T. M. Quinn, F. W. Taylor, T. Delcroix, and Y. Gouriou (2004), El Niño-
680 Southern Oscillation-related salinity variations recorded in the skeletal geochemistry of a
681 *Porites* coral from Espiritu Santo, Vanuatu, *Paleoceanography*, *19*(4),
682 doi:10.1029/2004PA001033.

683 Linsley, B. K., A. Kaplan, and Y. Gouriou (2006), Tracking the extent of the South Pacific
684 Convergence Zone since the early 1600s, *Geochem. Geophys. Geosyst.*, *7*,
685 doi:10.1029/2005GC001115.

686 Liu, Z., Z. Lu, X. Wen, B. L. Otto-Bliesner, A. Timmermann, and K. M. Cobb (2014), Evolution
687 and forcing mechanisms of El Niño over the past 21,000 years, *Nature*, *515*(7528), 550–553,
688 doi:10.1038/nature13963.

689 Marshall, J. F., and M. T. McCulloch (2002), An assessment of the Sr/Ca ratio in shallow water
690 hermatypic corals as a proxy for sea surface temperature, *Geochim. Cosmochim. Acta*,
691 *66*(18), 3263–3280, doi:10.1016/S0016-7037(02)00926-2.

692 Massey, F. J. (1951), The Kolmogorov-Smirnov test for goodness of fit, *J. Am. Stat. Assoc.*,
693 *46*(253), 68–78, doi:10.1080/01621459.1951.10500769.

694 Masson-Delmotte, V. et al. (2013), Information from paleoclimate archives, edited by T. F.
695 Stocker, D. Qin, G.-K. Plattner, M. Tignor, S. K. Allen, J. Boschung, A. Nauels, Y. Xia, V.
696 Bex, and P. M. Midgley, *Climate Change 2013: The Physical Science Basis. Contribution of*
697 *Working Group I to the Fifth Assessment Report of the Intergovernmental Panel on Climate*
698 *Change*.

699 McGregor, S., A. Timmermann, M. H. England, O. Elison Timm, and A. T. Wittenberg (2013),
700 Inferred changes in El Niño–Southern Oscillation variance over the past six centuries, *Clim.*
701 *Past*, *9*(5), 2269–2284, doi:10.5194/cp-9-2269-2013.

702 Moy, C. M., G. O. Seltzer, D. T. Rodbell, and D. M. Anderson (2002), Variability of El
703 Niño/Southern Oscillation activity at millennial timescales during the Holocene epoch,
704 *Nature*, *420*(6912), 159–162, doi:10.1038/nature01163.

705 Newton, A., R. Thunell, and L. Stott (2006), Climate and hydrographic variability in the Indo-
706 Pacific Warm Pool during the last millennium, *Geophys. Res. Lett.*, *33*(19), 596–5,
707 doi:10.1029/2006GL027234.

708 Nurhati, I. S., K. M. Cobb, C. D. Charles, and R. B. Dunbar (2009), Late 20th century warming
709 and freshening in the central tropical Pacific, *Geophys. Res. Lett.*, *36*(21), 345–4,
710 doi:10.1029/2009GL040270.

711 Okumura, Y. M., T. Sun, and X. Wu (2017), Asymmetric modulation of El Niño and La Niña
712 and the linkage to tropical Pacific decadal variability, *J. Climate*, *30*(12), 4705–4733,
713 doi:10.1175/JCLI-D-16-0680.1.

714 Parzen, E. (1962), On estimation of a probability density function and mode, *Ann. Math. Stat.*,
715   *33*(3), 1065–1076, doi:10.1214/aoms/1177704472.

716 Pearson, K. (1920), Notes on the history of correlation, *Biometrika*, *13*(1), 25,
717   doi:10.2307/2331722.

718 Quinn, T. M., and D. E. Sampson (2002), A multiproxy approach to reconstructing sea surface
719   conditions using coral skeleton geochemistry, *Paleoceanography*, *17*(4), 14–1–14–11,
720   doi:10.1029/2000PA000528.

721 Quinn, T. M., F. W. Taylor, and T. J. Crowley (2006), Coral-based climate variability in the
722   Western Pacific Warm Pool since 1867, *J. Geophys. Res.*, *111*(C11), 345–11,
723   doi:10.1029/2005JC003243.

724 Quinn, T. M., T. J. Crowley, and F. W. Taylor (1996), New stable isotope results from a 173-
725   year coral from Espiritu Santo, Vanuatu, *Geophys. Res. Lett.*, *23*(23), 3413–3416,
726   doi:10.1029/96GL03169.

727 Rayner, N. A., D. E. Parker, E. B. Horton, C. K. Folland, L. V. Alexander, and D. P. Rowell
728   (2003), Global analyses of sea surface temperature, sea ice, and night marine air temperature
729   since the late nineteenth century, *J. Geophys. Res.*, *108*(D14), 14–37,
730   doi:10.1029/2002JD002670.

731 Rein, B., A. Lückge, and F. Sirocko (2004), A major Holocene ENSO anomaly during the
732   Medieval period, *Geophys. Res. Lett.*, *31*(17), doi:10.1029/2004GL020161.

733 Reynolds, R. W., and T. M. Smith (1994), Improved global sea surface temperature analyses
734   using optimum interpolation, *J. Clim.*, *7*(6), 929–948, doi:10.1175/1520-
735   0442(1994)007<0929:IGSSTA>2.0.CO;2.

736 Ropelewski, C. F., and M. S. Halpert (1987), Global and regional scale precipitation patterns
737   associated with the El Niño/Southern Oscillation, *Mon. Weather Rev.*, *115*(8), 1606–1626,
738   doi:10.1175/1520-0493(1987)115<1606:GARSPP>2.0.CO;2.

739 Rustic, G. T., A. Koutavas, T. M. Marchitto, and B. K. Linsley (2015), Dynamical excitation of
740   the tropical Pacific Ocean and ENSO variability by Little Ice Age cooling, *Science*,
741   *350*(6267), 1537–1541, doi:10.1126/science.aac9937.

742 Santoso, A., M. J. McPhaden, and W. Cai (2017), The defining characteristics of ENSO
743   extremes and the strong 2015/2016 El Niño, *Rev. Geophys.*, *55*(4), 1079–1129,
744   doi:10.1002/2017RG000560.

745 Schmidt, G. A. et al. (2014), Using palaeo-climate comparisons to constrain future projections in
746   CMIP5, *Clim. Past*, *10*(1), 221–250, doi:10.5194/cp-10-221-2014.

747 Schrag, D. P. (1999), Rapid analysis of high-precision Sr/Ca ratios in corals and other marine
748   carbonates, *Paleoceanography*, *14*(2), 97–102, doi:10.1029/1998PA900025.

749 Shen, C.-C. et al. (2012), High-precision and high-resolution carbonate ^{230}Th dating by MC-ICP-
750   MS with SEM protocols, *Geochim. Cosmochim. Acta*, *99*(C), 71–86,
751   doi:10.1016/j.gca.2012.09.018.

752 Taylor, F. W., C. Fröhlich, J. Lecolle, and M. Strecker (1987), Analysis of partially emerged
753   corals and reef terraces in the central Vanuatu arc: Comparison of contemporary coseismic
754   and nonseismic with Quaternary vertical movements, *J. Geophys. Res.*, *92*, 4905–4933,
755   doi:10.1029/JB092iB06p04905.

756 Taylor, F. W., R. L. Edwards, G. J. Wasserburg, and C. Frohlich (1990), Seismic recurrence
757   intervals and timing of aseismic subduction inferred from emerged corals and reefs of the
758   Central Vanuatu (New Hebrides) Frontal Arc, *J. Geophys. Res.*, *95*(B1), 393–408,
759   doi:10.1029/JB095iB01p00393.

760 Thirumalai, K., A. Singh, and R. Ramesh (2011), A MATLAB™ code to perform weighted
761   linear regression with (correlated or uncorrelated) errors in bivariate data, *J. Geol. Soc.*
762   *India*, *77*(4), 377–380, doi:10.1007/s12594-011-0044-1.

763 Thirumalai, K., F. W. Taylor, C.-C. Shen, L. L. Lavier, C. Frohlich, L. M. Wallace, C.-C. Wu, H.
764   Sun, and A. K. Papabatu (2015), Variable Holocene deformation above a shallow subduction
765   zone extremely close to the trench, *Nat. Commun.*, *6*(1), 1–6, doi:10.1038/ncomms8607.

766 Thirumalai, K., J. N. Richey, T. M. Quinn, and R. Z. Poore (2014), *Globigerinoides ruber*
767   morphotypes in the Gulf of Mexico: A test of null hypothesis, *Sci. Rep.*, *4*(1), 423–7,
768   doi:10.1038/srep06018.

769 Thirumalai, K., J. W. Partin, C. S. Jackson, and T. M. Quinn (2013), Statistical constraints on El
770   Niño Southern Oscillation reconstructions using individual foraminifera: A sensitivity
771   analysis, *Paleoceanography*, *28*(3), 401–412, doi:10.1002/palo.20037.

772 Torrence, C., and G. Compo (1998), A practical guide to wavelet analysis, *Bull. Amer. Meteor.*
773   *Soc.*, *79*(1), 61–78, doi:10.1175/1520-0477(1998)079<0061:APGTWA>2.0.CO;2.

774 Trenberth, K. E. (1976), Spatial and temporal variations of the Southern Oscillation, *Q.J.R.*
775   *Meteorol. Soc.*, *102*(433), 639–653, doi:10.1002/qj.49710243310.

776 Trenberth, K. E. (1997), The definition of El Niño, *Bull. Amer. Meteor. Soc.*, *78*(12), 2771–2777,
777   doi:10.1175/1520-0477(1997)078<2771:TDOENO>2.0.CO;2.

778 Trenberth, K. E., and T. J. Hoar (1996), The 1990–1995 El Niño-Southern Oscillation event:
779   Longest on record, *Geophys. Res. Lett.*, *23*(1), 57–60, doi:10.1029/95GL03602.

780 Trenberth, K. E., J. M. Caron, D. P. Stepaniak, and S. Worley (2002), Evolution of El Niño–
781   Southern Oscillation and global atmospheric surface temperatures, *J. Geophys. Res.*, *107*,
782   doi:10.1029/2000JD000298.

783 Tudhope, A. W. (2001), Variability in the El Nino-Southern Oscillation through a glacial-
784   interglacial cycle, *Science*, *291*(5508), 1511–1517, doi:10.1126/science.1057969.

785 Vincent, E. M., M. Lengaigne, C. E. Menkes, and N. C. Jourdain (2011), Interannual variability
786   of the South Pacific Convergence Zone and implications for tropical cyclone genesis, *Clim*
787   *Dyn*, doi:10.1007/s00382-009-0716-3.

788 Wittenberg, A. T. (2009), Are historical records sufficient to constrain ENSO simulations?
789   *Geophys. Res. Lett.*, *36*(12), 3–5, doi:10.1029/2009GL038710.

790 Wolter, K., and M. S. Timlin (2011), El Niño/Southern Oscillation behaviour since 1871 as
791   diagnosed in an extended multivariate ENSO index (MEI.ext), edited by S. Gulev, *Int. J.*
792   *Climatol.*, *31*(7), 1074–1087, doi:10.1002/joc.2336.

793 **Figure Captions**

794 **Figure 1. Instrumental sea-surface temperature anomalies during strong ENSO events. a**
795 Average November-December-January (NDJ) sea-surface temperature anomalies (SSTA) for the
796 1972-73, 1982-83, and 1997-98 El Niño events. **b** Average NDJ SSTA for the 1988-89, 1995-96,
797 1998-99 La Niña events. SST data is from the Met Office Hadley Centre HadISST product [*Rayner*
798 *et al.*, 2003]. SSTA in this study are computed by applying a 9-year high-pass filter to monthly
799 SST data, removing the climatology, and calculating the 5-month running mean [*Trenberth*, 1997]
800 SSTA (Section 3.3). The Niño 3.4 region (5° N-5°S, 120°-170°W) in the central equatorial Pacific
801 is outlined by a white box (**a**, **b**). The modern coral site at Sabine Bank, Vanuatu in the southwest
802 Pacific (15.9°S, 166.0°E) is indicated with a star (**a**, **b**).

803 **Figure 2. Quantifying 20th century SST variability in the Niño 3.4 region. a** Instrumental
804 monthly SST [*Rayner et al.*, 2003] averaged over the Niño 3.4 region for 1900-2005 CE. **b**
805 Histogram (red) and probability density function (PDF) estimate (black) of the monthly SST for
806 1900-2005 CE. **c** Time series of monthly SSTA. Horizontal gray lines demarcate the 2.5 and 97.5
807 percentiles ($p_{2.5}$, $p_{97.5}$) of the monthly SSTA over the 1900-2005 CE interval. Red triangles indicate
808 historical El Niño events, blue triangles indicate La Niña events based on the Oceanic Niño index
809 (NOAA, Section 3.1) and the extended multivariate ENSO index [*Wolter and Timlin*, 2011]. The
810 selected ENSO events used to make the composite maps in Figure 1 are the larger triangles outlined
811 in black. **d** Histogram (red, bin = 0.5°C) and PDF estimate (black) of the monthly SSTA for 1900-
812 2005 CE. **e** The ±2σ range (dashed) and $p_{97.5} - p_{2.5}$ interpercentile range (solid) computed in 20-
813 year moving windows. **f** PDF estimates of SSTA for intervals with less (blue: 1920-1939 CE) and
814 more (red: 1980-1999 CE) ENSO variability. Blue (red) shading in (**c, e**) highlight the intervals in
815 **f** with less (more) ENSO variability. Numerical values above the PDFs in (**d, f**) denote the 2.5 and
816 97.5 percentiles for the designated subset interval. The horizontal bars above the PDFs in (**d, f**)
817 indicate the $p_{97.5} - p_{2.5}$ interpercentile range. Monthly SSTA calculated using the same
818 methodology as Figure 1 (Section 3.3). PDFs in this and all subsequent figures are based on a
819 kernel density estimation method [*Parzen*, 1962].

820 **Figure 3. Quantifying 20th century instrumental SST variability at Vanuatu (SW Pacific).**
821 The number of observations per month in the 5° latitude x 5° longitude HadSST3 [*Kennedy et al.*,
822 2011a; 2011b] grid box (17.5°S, 167.5°E) that includes Vanuatu. Note the logarithmic scale for
823 the number of observations per month and the horizontal gray lines that indicate the number of
824 observations required to achieve specified temporal coverages. The amplitude of SST variability
825 outside of the monthly mean-removed climatology is loosely tied to the number of observations,
826 such that more observations lead to more interannual, and even decadal, SST variability. **b**

827 Instrumental monthly SST [*Rayner et al.*, 2003] and **c** the histogram (blue, bin = 0.5 °C) and PDF
828 (black) of monthly SST for Vanuatu. The SST data are the average of the two grid points closest
829 to the coral sites (15.5°S, 166.5°E) and (16.5°S, 166.5°E; Section 3.1). **d** Instrumental monthly
830 SSTA. Horizontal gray lines demarcate the $p_{2.5}$ and $p_{97.5}$ monthly SSTA values for the 1900-2005
831 CE interval. Red triangles indicate El Niño events and blue triangles indicate La Niña events as in
832 Fig. 2c. **e** Histogram (blue, bins = 0.5 °C) and PDF (black) of monthly SSTA for the 1900-2005
833 CE interval. **f** The ±2σ range (dashed) and $p_{97.5} - p_{2.5}$ interpercentile range (solid) of monthly SSTA
834 computed in 20-year moving windows. **g** PDF estimates of monthly SSTA for intervals with less
835 (blue: 1920-1939 CE) and more (red: 1980-1999 CE) ENSO variability observed in the Niño 3.4
836 region (Fig. 2). Monthly SSTA computed the same as Fig. 1 (Section 3.3). The numerical values
837 and horizontal bar above the PDF in **e**, **g** indicate the ~ ±2σ range as defined by the percentiles.
838
839 **Figure 4. Quantifying 20th century SST variability in the SW Pacific using modern corals. a**
840 Reconstructed monthly SST based on modern coral Sr/Ca from Sabine Bank, Vanuatu (15.9°S,
841 166.0°E). Monthly SST (total variability) shows a shift toward warmer SST due to a late 20th
842 century warming trend in the coral Sr/Ca time series. **b** Histogram (orange, bin = 0.5 °C) and PDF
843 (black) of monthly SST over the 1900-2005 CE interval. **c** Coral-based monthly SSTA. Horizontal
844 gray lines demarcate the $p_{2.5}$ and $p_{97.5}$ monthly SSTA values for the 1900-2005 CE interval. Red
845 triangles indicate El Niño events and blue triangles indicate La Niña events as in Fig. 2c. **d**
846 Histogram (orange, bins = 0.5 °C) of monthly SSTA for 1900-2005 CE. **e** The ±2σ range (dashed)
847 and $p_{97.5} - p_{2.5}$ interpercentile range (solid) of monthly SSTA computed in 20-year moving
848 windows. **f** PDF estimates of monthly SSTA for the intervals with less (blue: 1920-1939 CE) and
849 more (red: 1980-1999 CE) ENSO variability observed in the Niño 3.4 region (Fig. 2). The
850 numerical values and horizontal bar above the PDFs in **d**, **f** indicate the ~ ±2σ range as defined by
851 the 2.5 and 97.5 percentiles. Blue (red) shading in (**c, e**) highlight the intervals in **f** with less (more)
852 ENSO variability (Fig. 2). Monthly SSTA computed the same as Fig. 1 (Section 3.3). The
853 uncertainty in the 2.5 and 97.5 percentiles in (**d, f**) is ±0.21 °C based on analytical, calibration, and
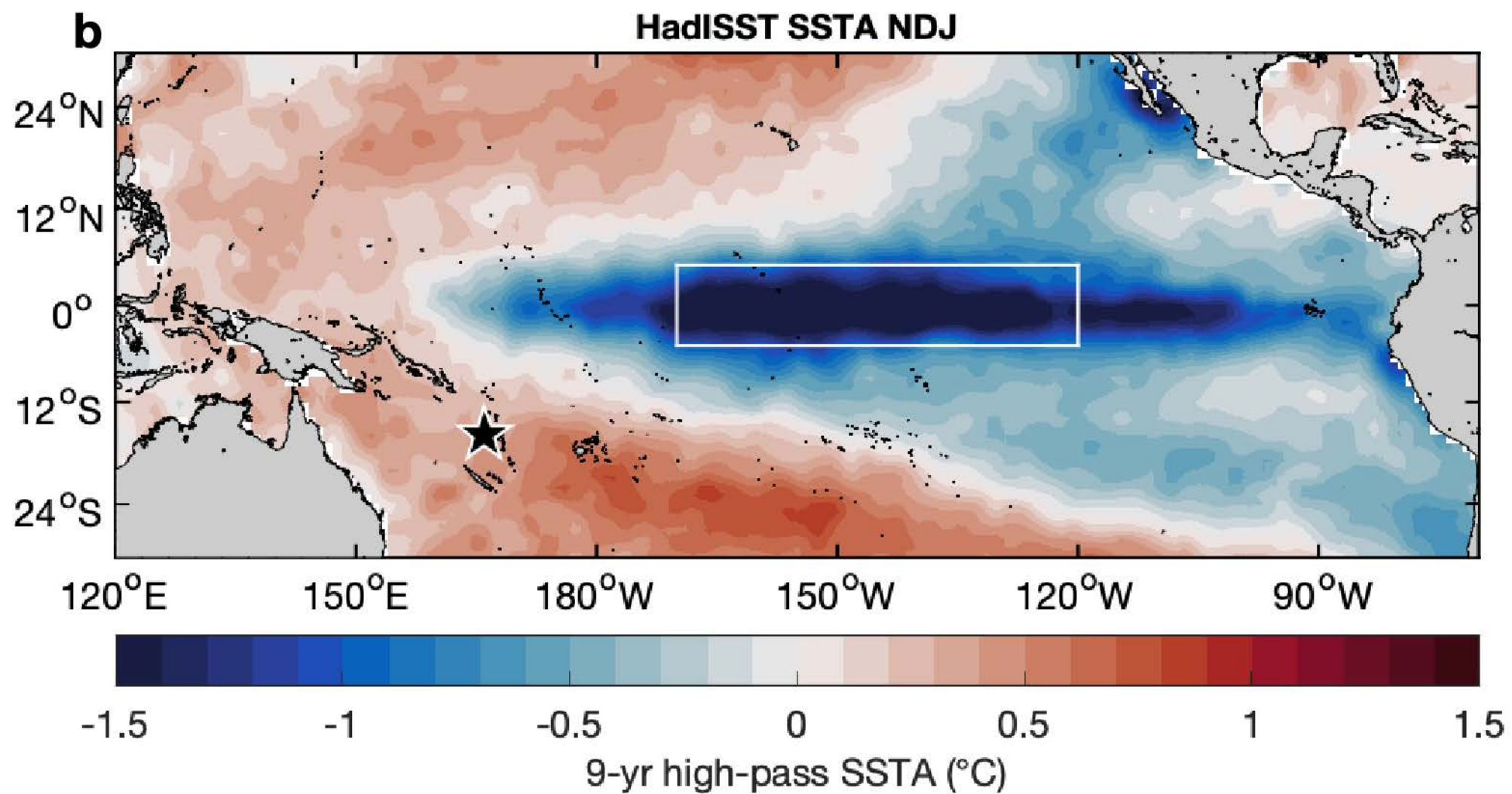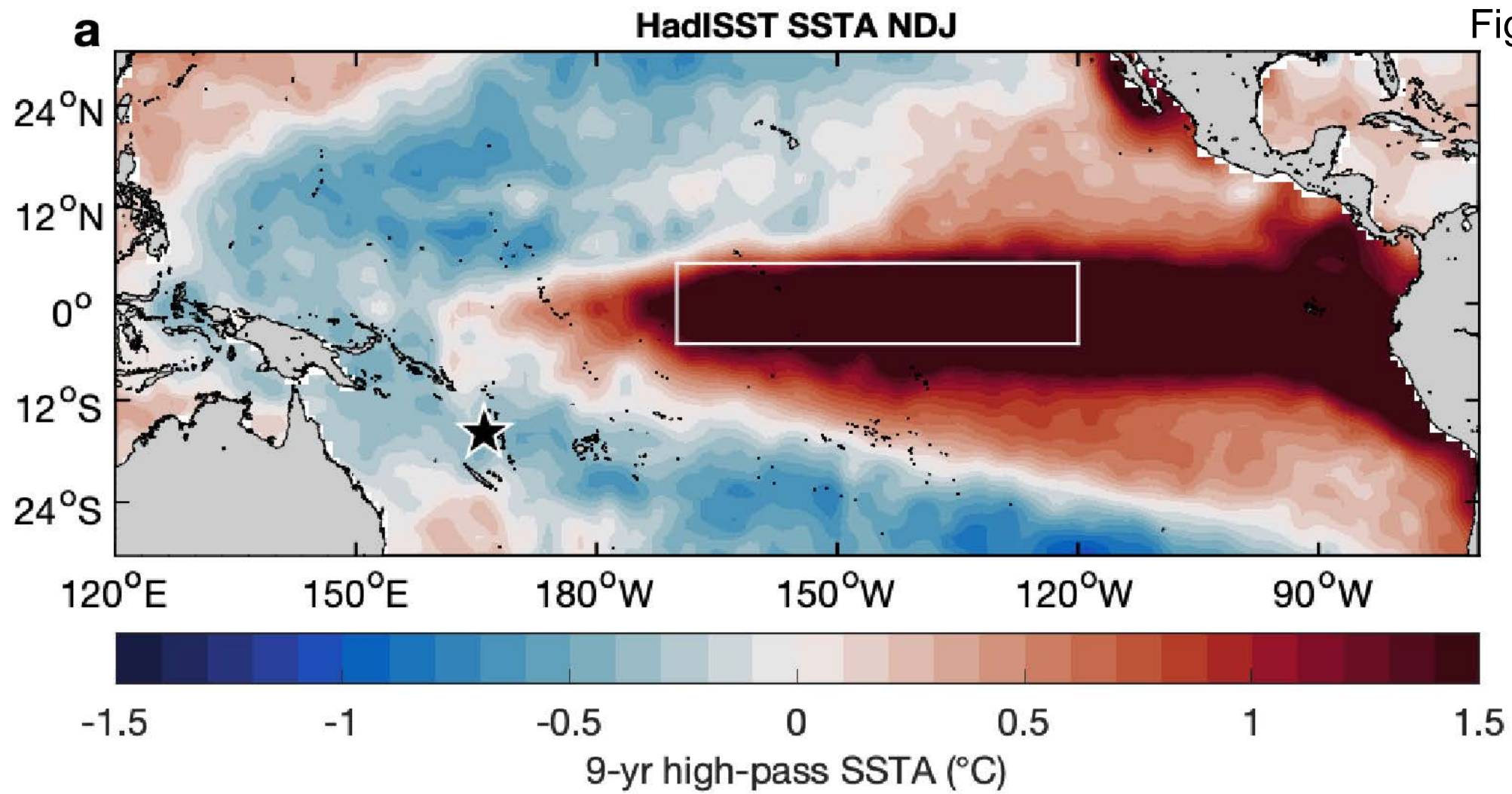854 replication uncertainties (Section 3.4).
855
856 **Figure 5. Quantifying Medieval Climate Anomaly SST variability in the SW Pacific using**
857 **fossil corals. a** Reconstructed monthly SST based on fossil coral Sr/Ca from Tasmaloum, Vanuatu
858 (15.6°S, 166.9°E). Coral 11-TM-S5 (green; ²³⁰Th ± 2σ age: 1127.1 ± 2.7 CE) and 11-TM-I1 (gray;
859 ²³⁰Th ± 2σ ages: 1125.7 ± 6.2, 1142.6 ± 4.9, 1149.0 ± 4.1 CE). Triangles with horizontal bars mark
860 the ²³⁰Th ages and ±2σ analytical error (see Section 2.3 for a description of the fossil coral
861 alignment). **b** Histogram (green, bin = 0.5 °C) and PDF (black) of monthly SST over the 1051-
862 1150 CE interval. **c** Coral-based monthly SSTA. Horizontal gray lines demarcate the $p_{2.5}$ and $p_{97.5}$
863 monthly SSTA values for the 1051-1150 CE interval. **d** Histogram (green, bins = 0.5 °C) of
864 monthly SSTA for the 1051-1150 CE interval. **e** The ±2σ range (dashed) and $p_{97.5} - p_{2.5}$
865 interpercentile range (solid) of monthly SSTA computed in 20-year moving windows. The
866 numerical values and horizontal bar above the PDF in **d** indicate the ~ ±2σ range as defined by the
867 2.5 and 97.5 percentiles. Monthly SSTA computed the same as Fig. 1 (Section 3.3). The
868 uncertainty in the 2.5 and 97.5 percentiles in (**d, f**) is ±0.24 °C based on analytical, calibration, and
869 replication uncertainties (Section 3.4).
870
871 **Figure 6. Modern and MCA fossil coral SSTA replication.** PDFs of monthly SSTA for the
872 modern and MCA corals over their respective common intervals of overlap. **a** Replication results
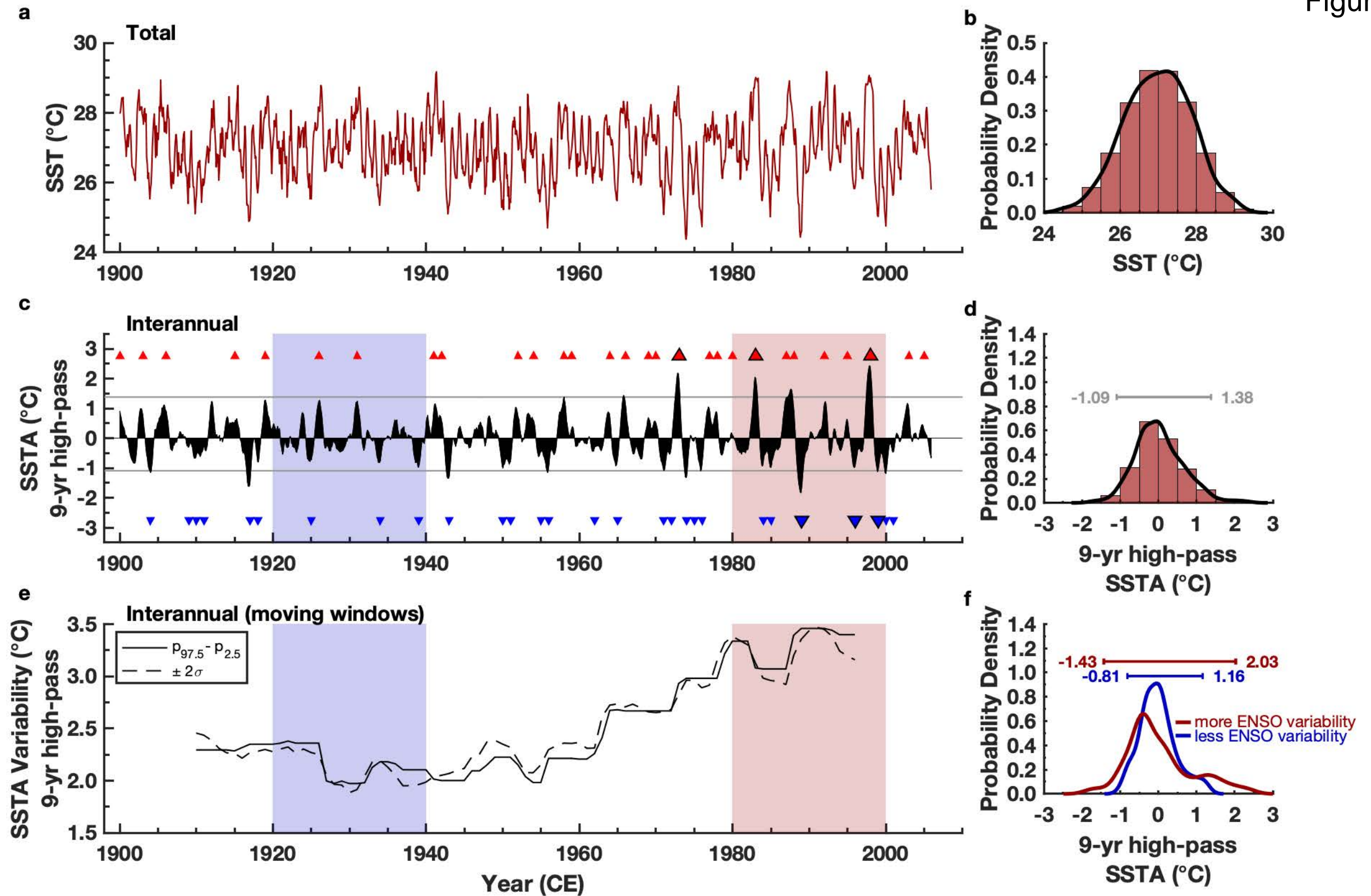
873 for 50 years (1941-1990 CE) of modern monthly SSTA data. PDF estimates for Sabine Bank
874 (orange) and Malo Channel [*Kilbourne et al.*, 2004] (gray), Vanuatu. **b** Replication results for 20
875 years (1126-1145 CE) of MCA fossil coral monthly SSTA data from Tasmaloum, Vanuatu. 11-
876 TM-S5 (green) and 11-TM-I1 (gray). Monthly SSTA computed the same as Fig. 1 (Section 3.3).
877 Numerical values and horizontal bars above the PDFs in **a**, **b** indicate ~ ±2σ range as defined by
878 the 2.5 and 97.5 percentiles. The uncertainty in the 2.5 and 97.5 percentiles is ±0.21 °C (**a**) and
879 ±0.24 °C (**b**) based on analytical, calibration, and replication uncertainties (Section 3.4).
880
881 **Figure 7. Coral-based ENSO variability comparison: Modern vs. MCA.** PDF estimates of
882 monthly SSTA (reconstructed from SW Pacific coral Sr/Ca) for the more (red) and less (blue)
883 variable ENSO intervals during the 20th century (from Fig. 4f) and 100 years during the MCA
884 (green; from Fig. 5d). Numerical values and horizontal bars above the PDFs indicate ~ ±2σ range
885 as defined by the 2.5 and 97.5 percentiles. The uncertainty in the 2.5 and 97.5 percentiles is ±0.21
886 °C (modern) and ±0.24 °C (MCA) based on analytical, calibration, and replication uncertainties
887 (Section 3.4).

Figure 1

a HadISST SSTA NDJ

b HadISST SSTA NDJ

9-yr high-pass SSTA (°C)

Figure 2

a Total

b

c Interannual

d

-1.09   1.38

e Interannual (moving windows)

p_{97.5} - p_{2.5}
±2σ

f

-1.43   2.03
-0.81   1.16

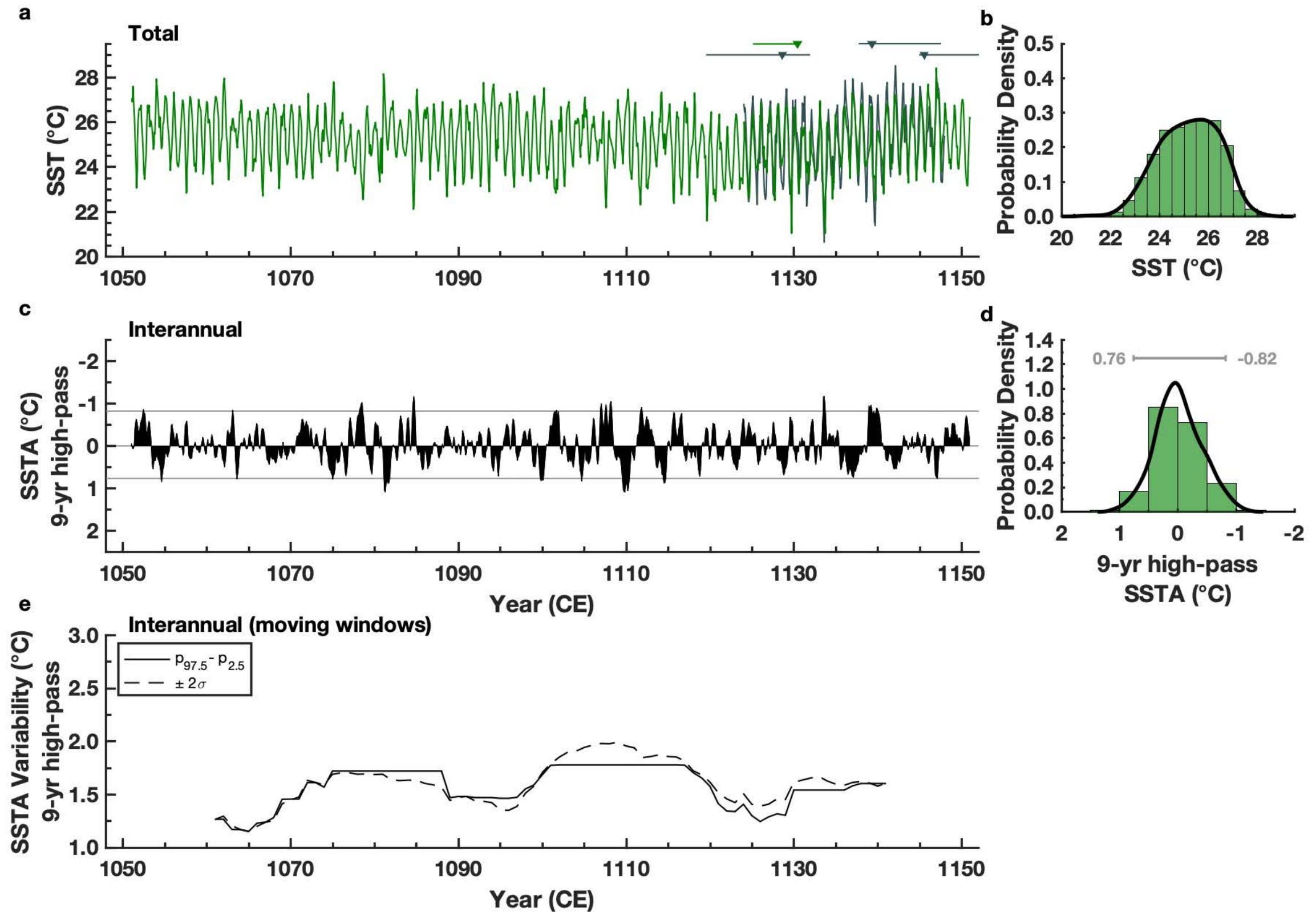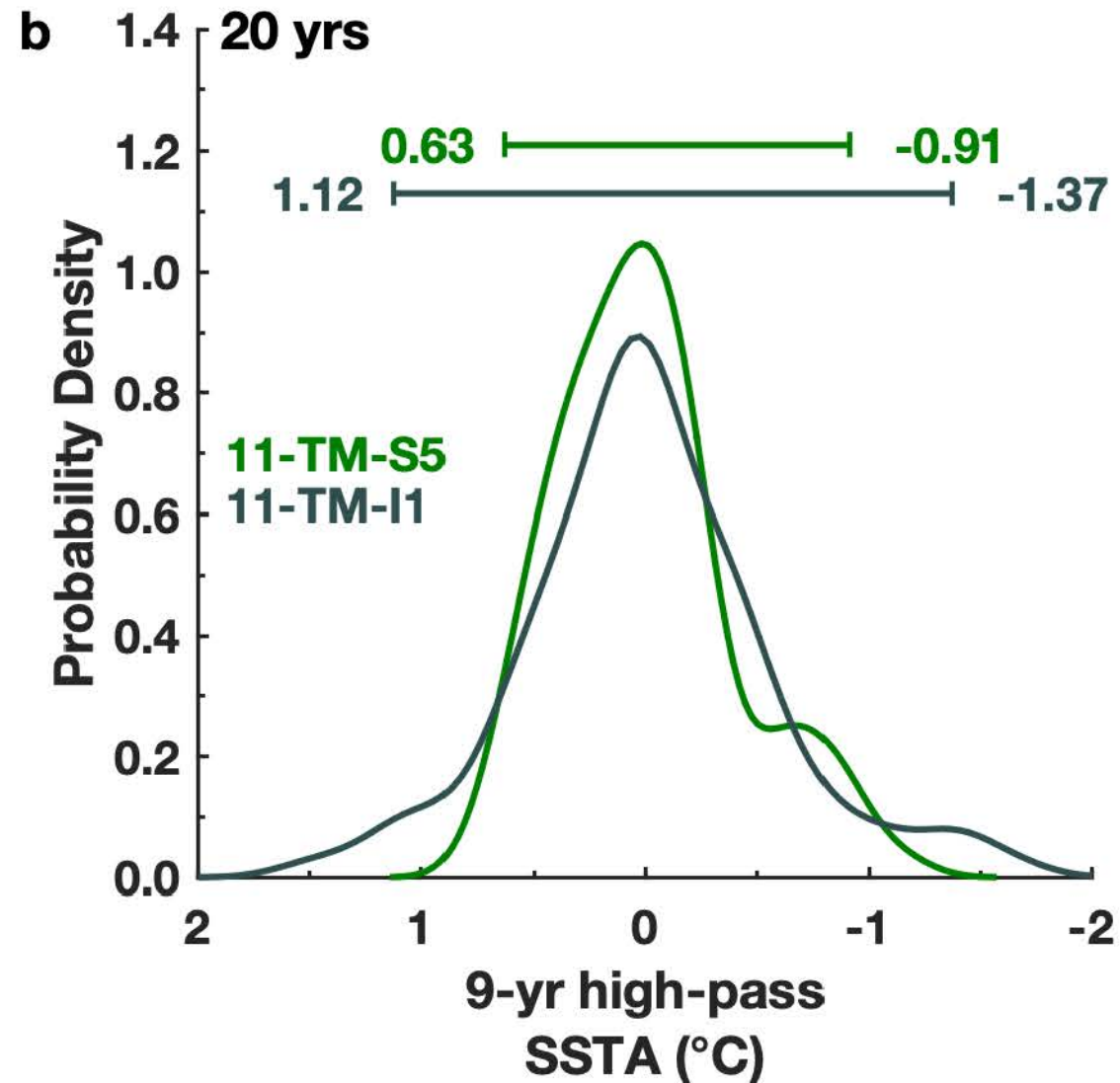more ENSO variability
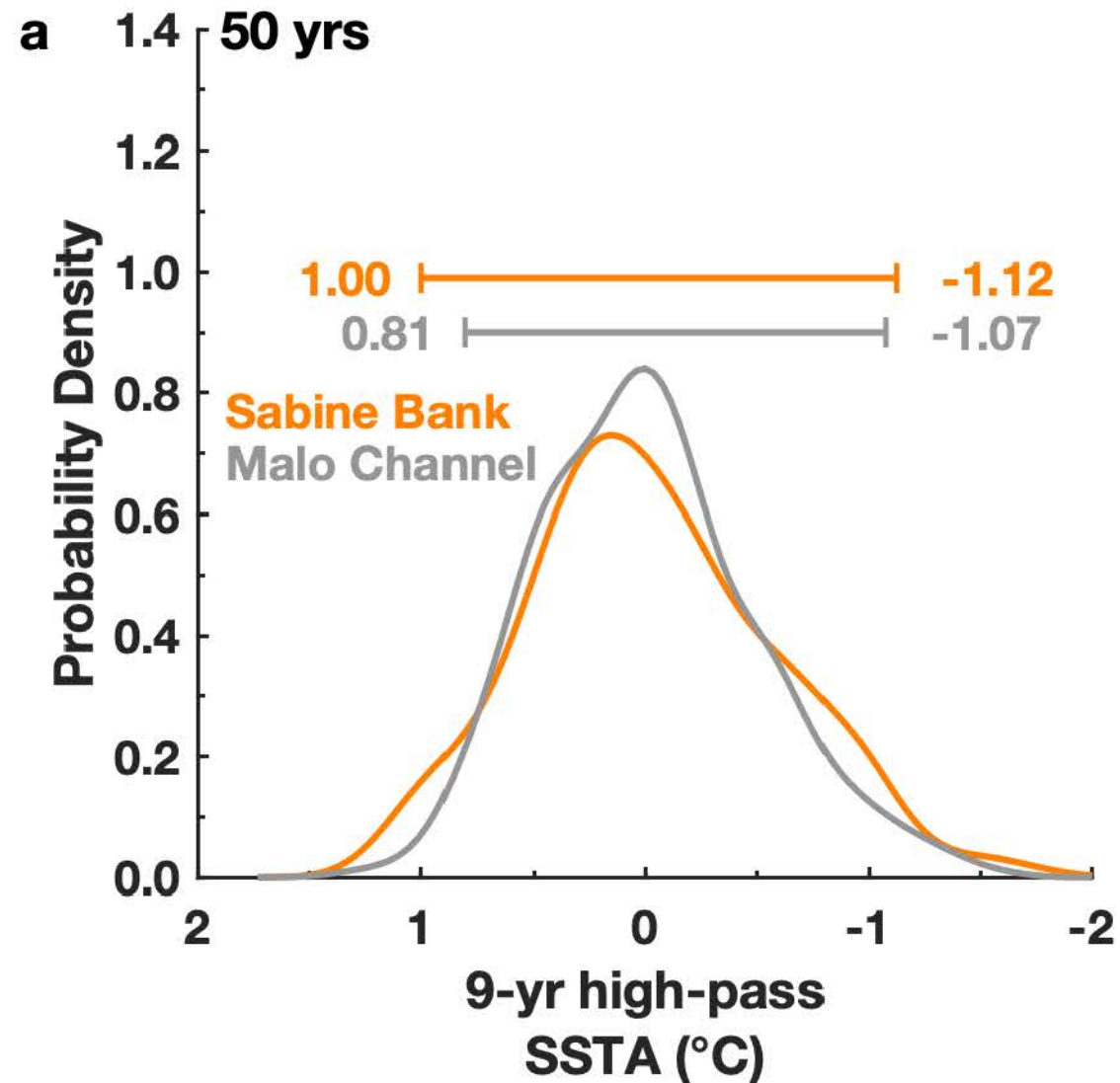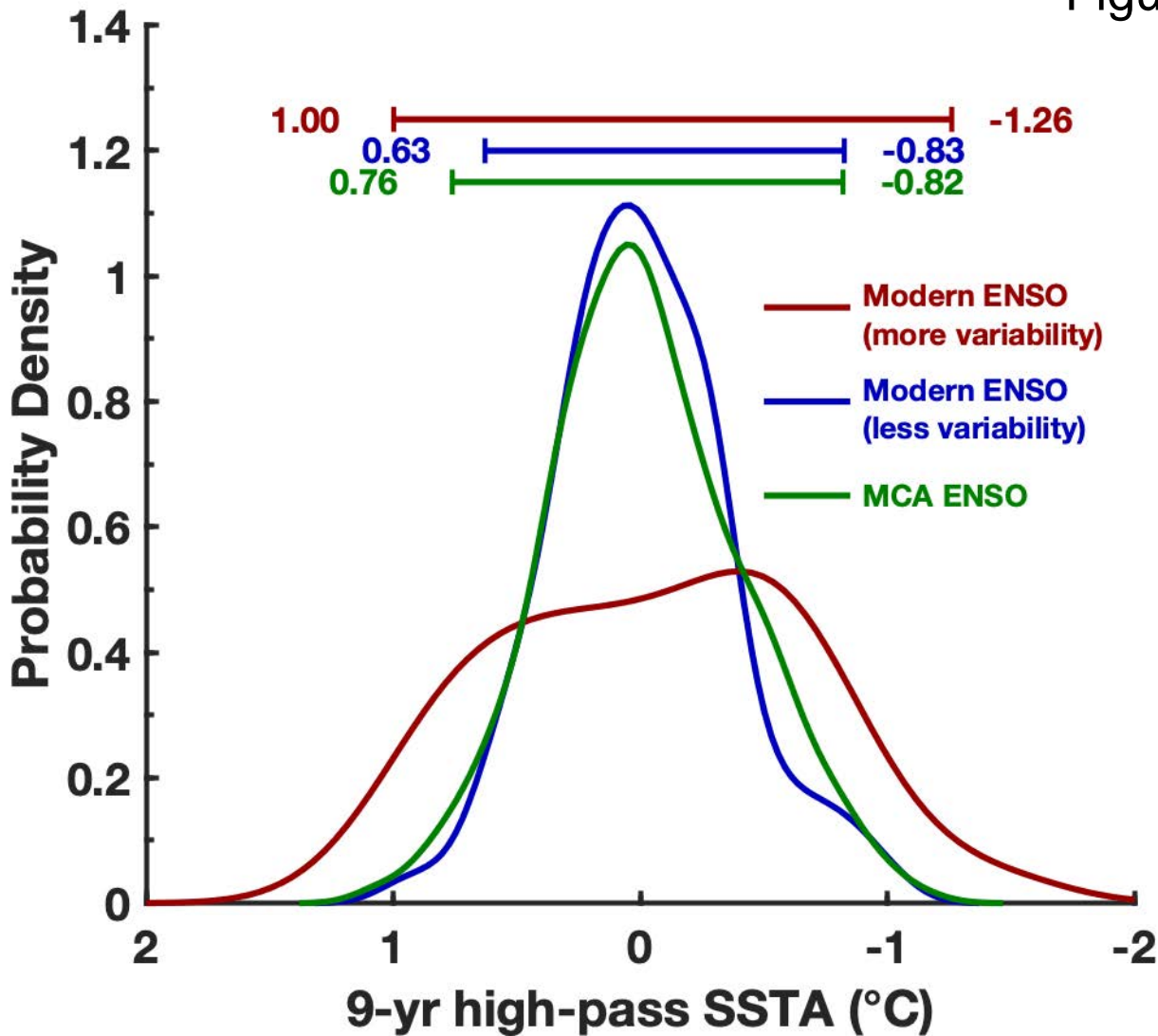less ENSO variability

Year (CE)

Figure 3
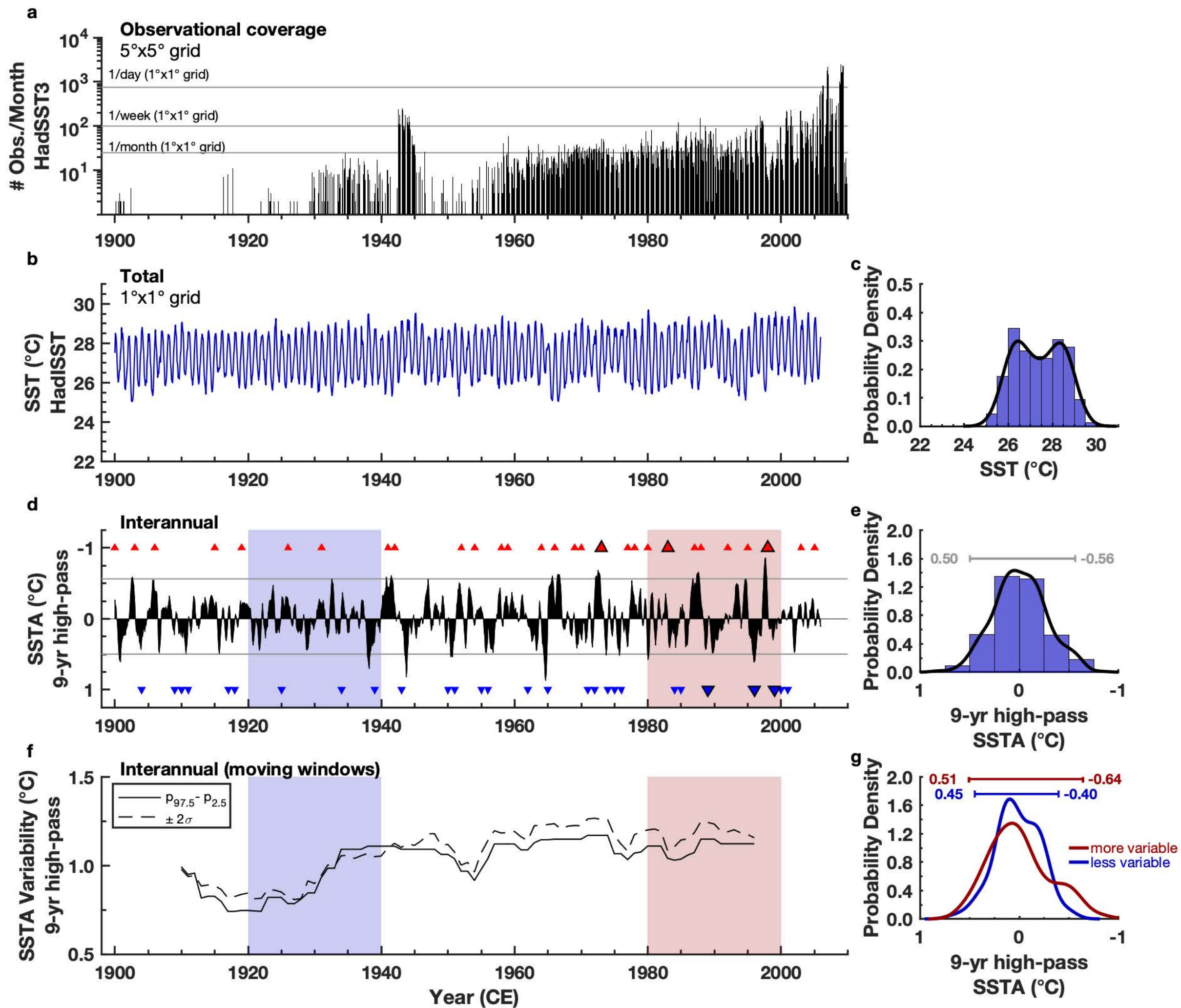
Figure 4
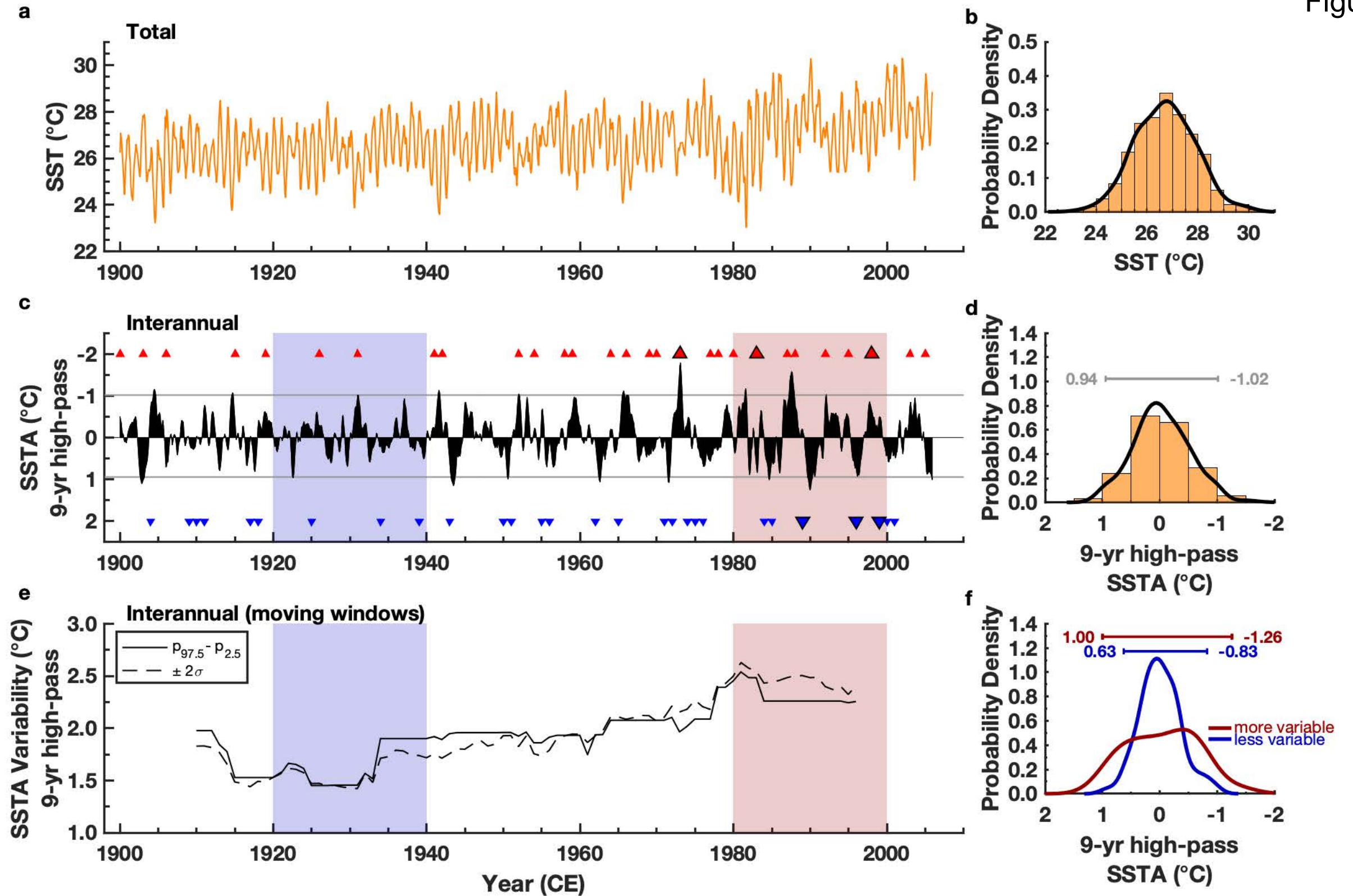
Figure 5

Figure 6

Figure 7

A century of reduced ENSO variability during the Medieval Climate Anomaly

A.E. Lawman[1,2]*, T.M. Quinn[1,2], J.W. Partin[1], K. Thirumalai[1,3], F.W. Taylor[1], C.-C. Wu[4,5], T.-.L Yu[4,5], M.K. Gorman[1,2], C.-C. Shen[4,5]

[1]Institute for Geophysics, Jackson School of Geosciences, The University of Texas at Austin, Austin, TX, USA, [2]Department of Geological Sciences, Jackson School of Geosciences, The University of Texas at Austin, Austin, TX, USA, [3]Department of Earth, Environmental and Planetary Sciences, Brown University – Providence, RI, USA, [4]High-precision Mass Spectrometry and Environment Change Laboratory (HISPEC), National Taiwan University, Taipei, Taiwan ROC, [5]Research Center for Future Earth, National Taiwan University, Taipei, Taiwan ROC

Contents of this file

Introduction

The supporting information contains analysis that demonstrates the response of southwest Pacific sea-surface temperature (SST) anomalies to individual ENSO events in the instrumental record (Figure S1) to highlight the consistent relationship between the southwest Pacific and SST in the Niño 3.4 region. The supporting information also includes metadata about the modern and fossil corals, including x-ray images (Figure S2, Table S1). Tables S2-S3 provide the information for the [230]Th age calculation for the fossil corals. The supporting information covers the results of the calibration-verification exercise for converting coral Sr/Ca measurements into SST (Figure S3). The agreement between the replicated MCA fossil coral Sr/Ca time series is provided (Figure S4). An example of the output from the Monte Carlo uncertainty quantification algorithm is provided for the Sabine Bank, Vanuatu modern coral Sr/Ca-SST reconstruction (Figure S5). The fidelity of the differences in the 2.5 and 97.5 percentile SSTA populations, or the magnitude of extreme events, is explored for the modern and MCA (Figures S6-S8). An informal test of the 'Wittenberg effect' [*Wittenberg*, 2009] is performed to show how the values for extreme events may vary according to window length (Figure S9).
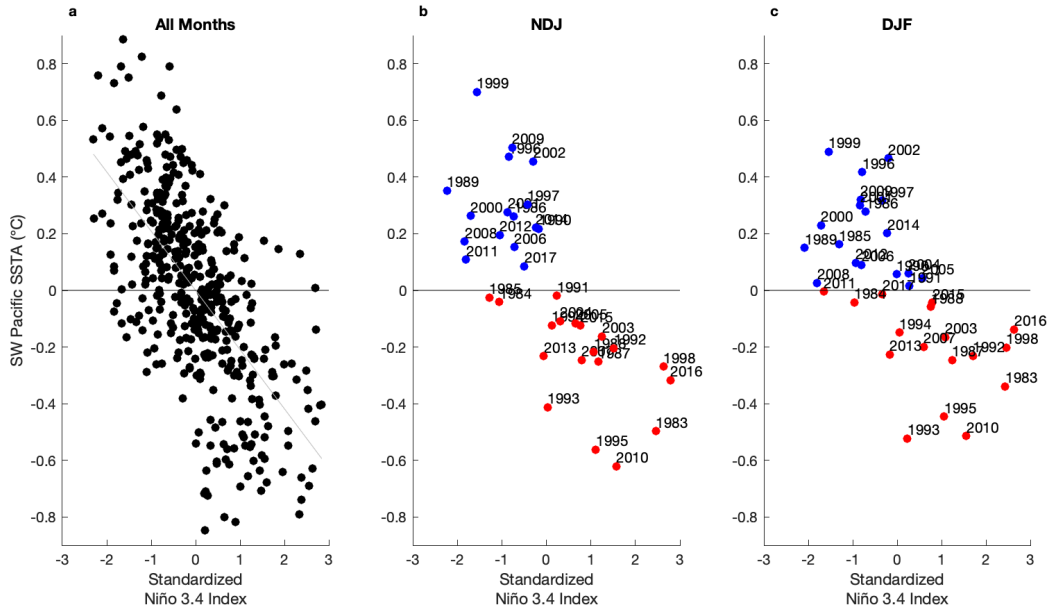
Figure S1. The southwest Pacific SST response to ENSO. Regression of southwest (SW) Pacific SST anomalies versus the standardized Niño 3.4 index for 1982-2018 CE. **a** All months. **b** The November-December-January (NDJ) average. **c** The December-January-February (DJF) average. SST data is from the Met Office Hadley Centre HadISST product [*Rayner et al.*, 2003]**,** and is subset to 1982-2018 CE to focus on the most recent decades of observations. Text labels in (**b, c**) indicate the year of the January in the average (e.g., 1998 indicates the average SST response for Nov. 1997, Dec. 1997, and January 1998; i.e., the 1997-98 El Niño. Blue markers indicate when the Niño 3.4 index is less than 0, red markers indicate when the Niño 3.4 index is greater than 0. The southwest Pacific cools during canonical eastern Pacific El Niño events (e.g., 1982-83, 1997-98, 2015-16) as well as moderate central Pacific events (e.g., 1994-95 and 2009-10). The Niño 3.4 region in the central equatorial Pacific is defined by (5° N-5°S, 120°-170°W). The southwest Pacific is defined by the region (12°-22°S, 166-178°E), which includes Vanuatu. SST anomalies are calculated with respect to the 1982-2018 CE climatology. We note that the SST anomalies here are not 9-year high-pass filtered and are thus not directly comparable to the amplitude of the SST anomalies shown in Figure 3d in the main text. Despite the varied response of the SW Pacific to different types of ENSO events, the SW Pacific consistently cools (warms) during historical El Niño (La Niña) events.

a Modern
06-SB-A1

b Fossil
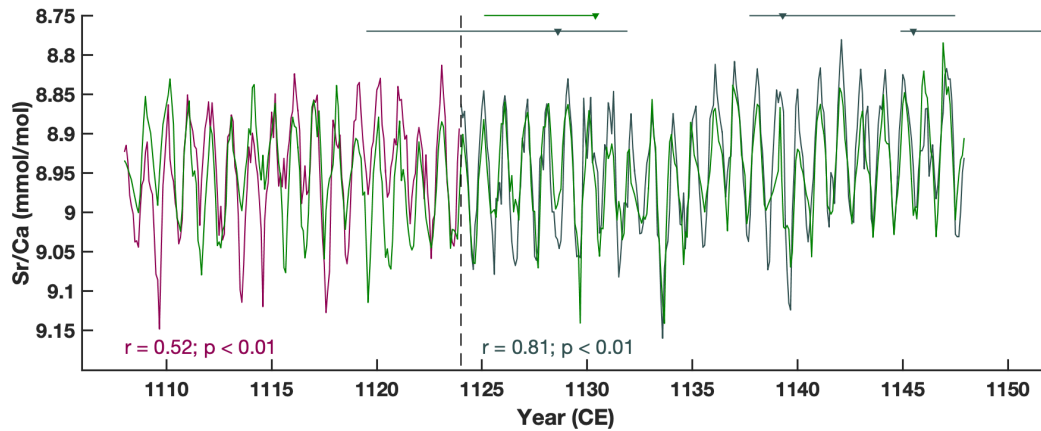11-TM-S5

c Fossil
11-TM-I1

5 cm
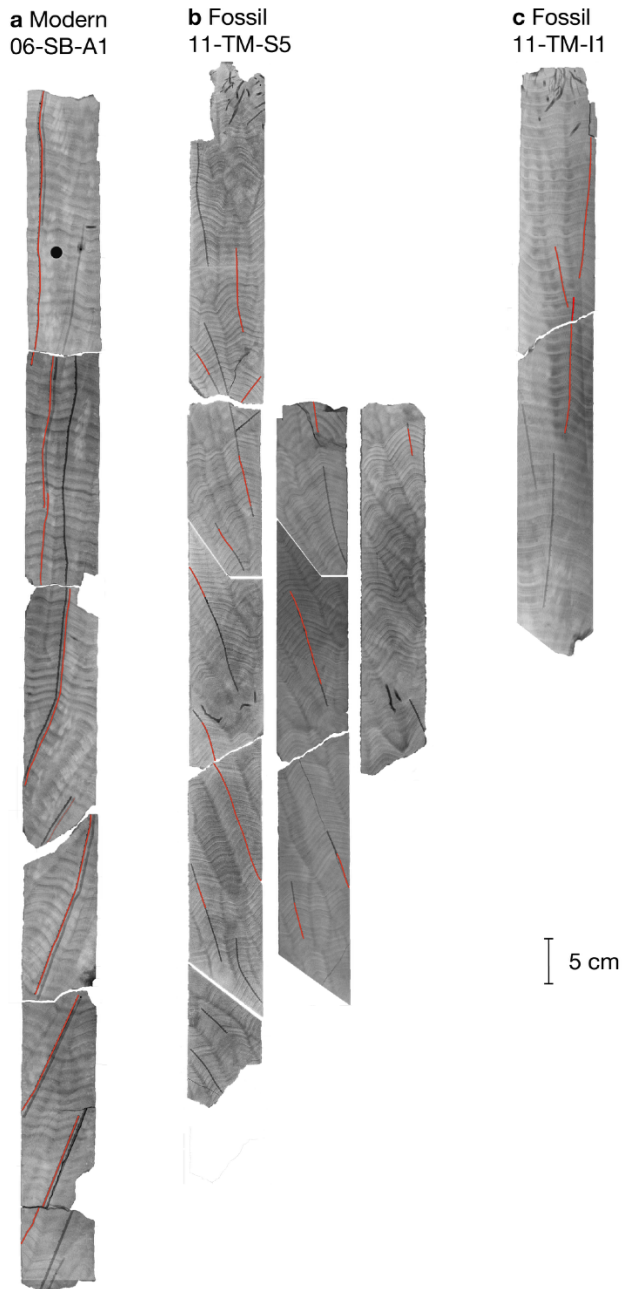
Figure S2. Coral x-radiographs and sampling paths. X-ray images of 5 mm thick slabs from modern coral 06-SB-A1 (**a**), fossil coral 11-TM-S5 (**b**), and fossil coral 11-TM-I1 (**c**). The modern core in a was collected from a live *Porites lutea* coral head at Sabine Bank, Vanuatu during a drilling expedition in 2006. The fossil corals in **b, c** were collected from the same uplifted reef at Tasmaloum, Vanuatu but from different coral heads during a drilling expedition in 2011. The adjacent slabs to the right of the first slabs in **b** are additional cross-sectional slabs taken from the core to fill in gaps with suboptimal sampling. The solid red lines indicate sampling paths along the coral's maximum growth axis. The non-colored paths indicate suboptimal sampling paths [*DeLong et al.*, 2013]. The final composite includes data only from the red paths. Scale bar represents 5 cm.
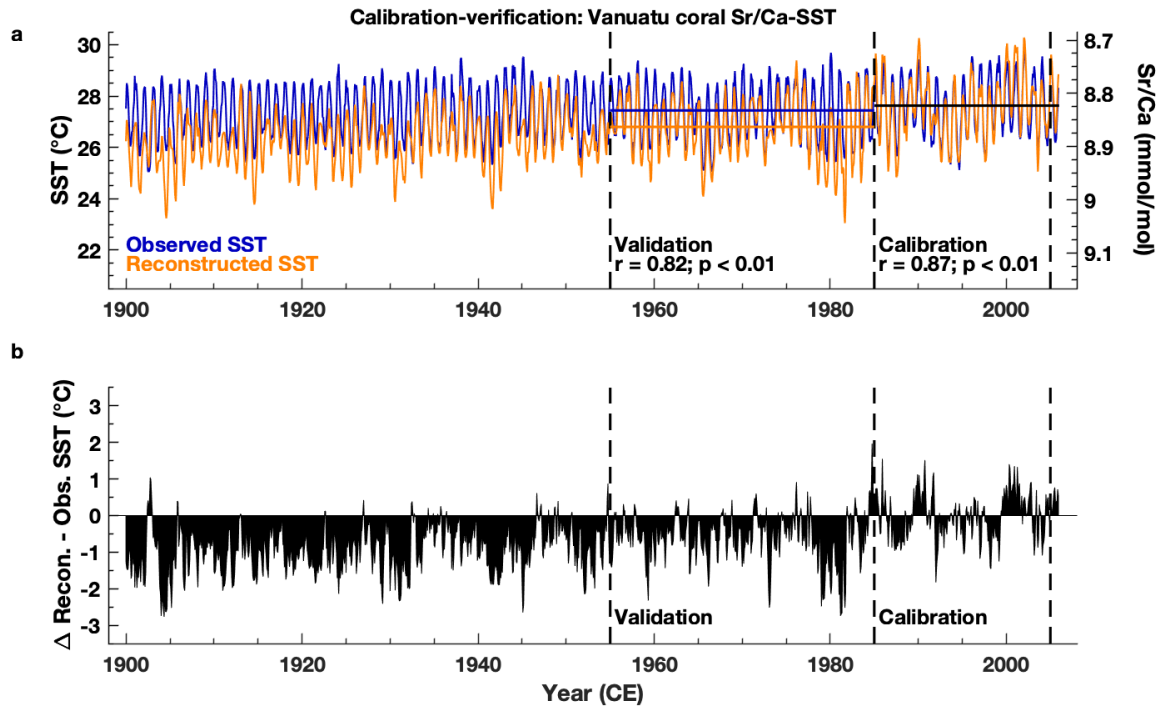
Figure S3. Modern coral SST calibration and verification. a Instrumental SST [*Rayner et al.*, 2003] (blue, see Fig. 3) and reconstructed Sabine Bank, Vanuatu (15.9°S, 166.0°E) modern coral Sr/Ca-SST (orange; Fig. 4; Section 3.2). Left axis SST (°C), right axis coral Sr/Ca (mmol/mol). Dashed vertical lines mark the calibration (1985-2005 CE) and verification (1955-1984 CE) intervals (Section 3.2). The black horizontal line indicates the observed/reconstructed median SST value over the calibration window. The colored horizontal lines indicate the median SST values over the verification windows for observed SST (blue) and reconstructed coral Sr/Ca-SST (orange). Calibration equation: SST (°C) = -20.73 x Coral Sr/Ca (mmol/mol) + 210.53. The 1985-2005 CE calibration interval maximizes the correlation [*Pearson*, 1920] with instrumental SST ($r = 0.87$, $p < 0.01$) and minimizes the residual sum of squares over the 1955-1984 CE verification window (Section 3.2). **b** The difference between the modern Sabine Bank coral SST reconstruction and observed SST. Much of the difference on interannual to decadal timescales stems from the lack of observations (Fig. 3), including the smaller global warming trend in observations, as compared to the coral. The coral trend of 0.83 °C/50 years at Sabine Bank resembles the trend of 0.5-0.75°C/50 years seen in observations for the southwest Pacific [*Cravatte et al.*, 2009].

Figure S4. Replicated fossil coral Sr/Ca during part of the Medieval Climate Anomaly. Sr/Ca time series for fossil coral 11-TM-S5 (green; [230]Th ± 2σ age: 1127.1 ± 2.7 CE) and the shorter replication coral 11-TM-I1 ([230]Th ± 2σ ages: 1125.7 ± 6.2, 1142.6 ± 4.9, 1149.0 ± 4.1 CE) over their common interval of overlap (1108-1147 CE). Section of 11-TM-I1 data that passed the quality control metrics outlined by *DeLong et al.* [2013] (gray, 1124-1147 CE) and is included in the final Sr/Ca composite. Section of 11-TM-I1 data that did not pass the quality control metrics (magenta, 1108-1123 CE) due to stress banding and a lack of clearly defined theca walls that help identify the maximum growth axis in the x-ray image (Figure S1). Dashed vertical black line separates the sections with optimal and sub-optimal sampling of 11-TM-I1. To yield a reliable climate reconstruction, sections with sub-optimal sampling are excluded from the final coral records presented in the main text. Triangles with horizontal bars mark the [230]Th ages and ±2σ analytical error. The fossil coral Sr/Ca time series were shifted within the analytical error (±2σ) of the four [230]Th ages such that the resulting overlap between 11-TM-S5 and 11-TM-I1 achieved the highest Pearson correlation coefficient [*Pearson*, 1920] (r = 0.81, p < 0.01) over the 1124-1147 CE interval that includes coral data that passed all quality control metrics. The Pearson correlation coefficient is lower (r = 0.52) for the 1108-1123 CE interval that includes data from 11-TM-I1 that did not pass all quality control metrics.
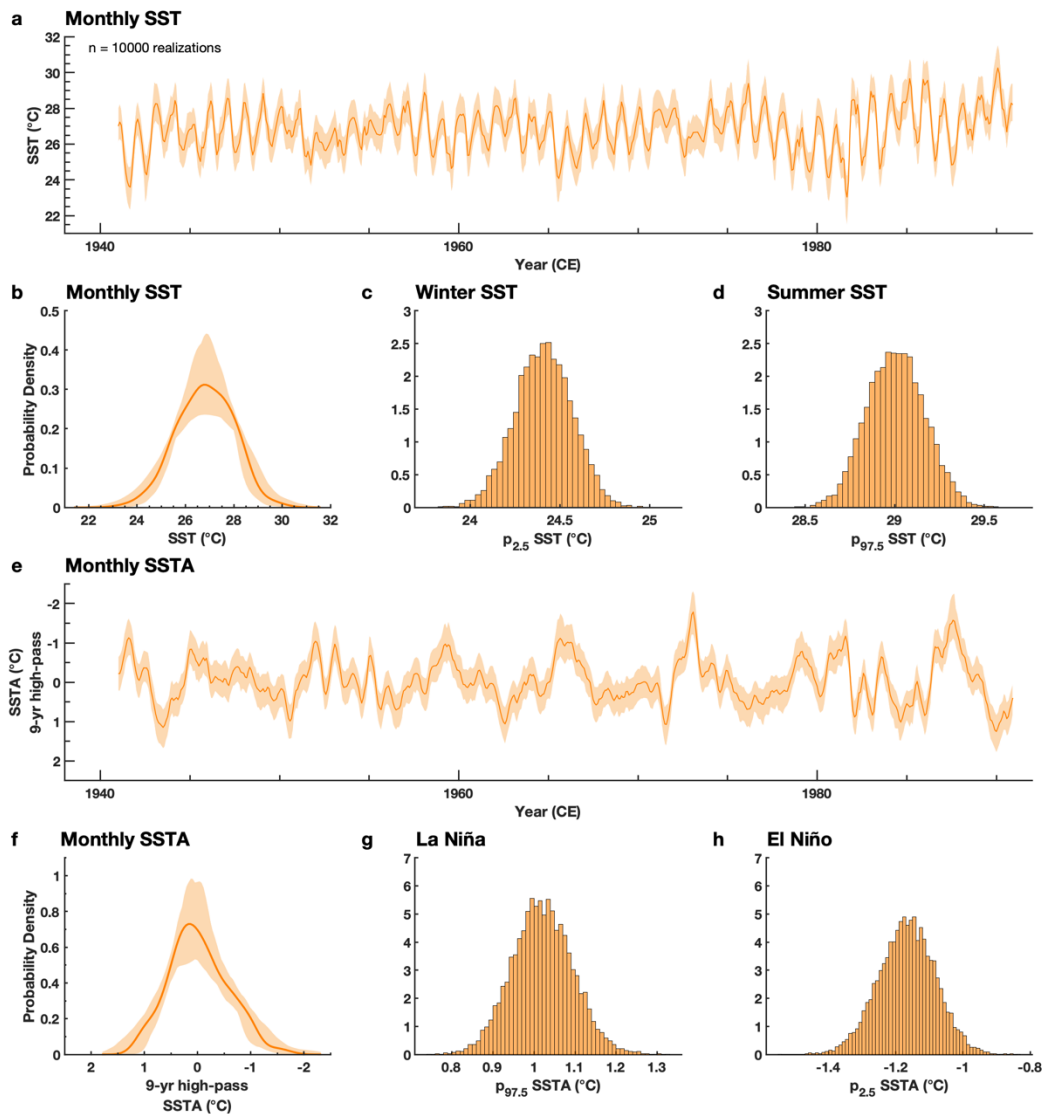
Figure S5. Monte Carlo uncertainty quantification for modern coral Sr/Ca-SST. a The modern Sabine Bank Sr/Ca-SST reconstruction for the 1941-1990 CE replication interval with no uncertainty (dark orange) and with realizations (light orange shading) that take analytical and calibration uncertainty into account (n = 10,000 realizations; Section 3.4). **b** PDF estimate of the SST reconstruction (dark orange) with realizations (light orange). **c, d** Histograms showing the distribution of possible $p_{2.5}$ (**c**) and $p_{97.5}$ (**d**) SST values based on 10,000 realizations of the SST series. **e** Realizations of the modern Sabine Bank SSTA series (light orange shading) with the SSTA reconstruction with no uncertainty (dark orange). **f** PDF estimates of the SSTA realizations (light orange) and no uncertainty (dark orange). **g, h** Histograms showing the distribution of $p_{97.5}$ (**g**) and $p_{2.5}$ (**h**) SSTA values. Monthly anomalies are computed by applying a 9-year high-pass filter to the SST data, removing the climatology, and computing the 5-month running mean SSTA (Section 3.3). The uncertainty in the SSTA percentiles due to analytical and calibration uncertainty is the average ±2σ value (±0.15 °C) from **g, h**.
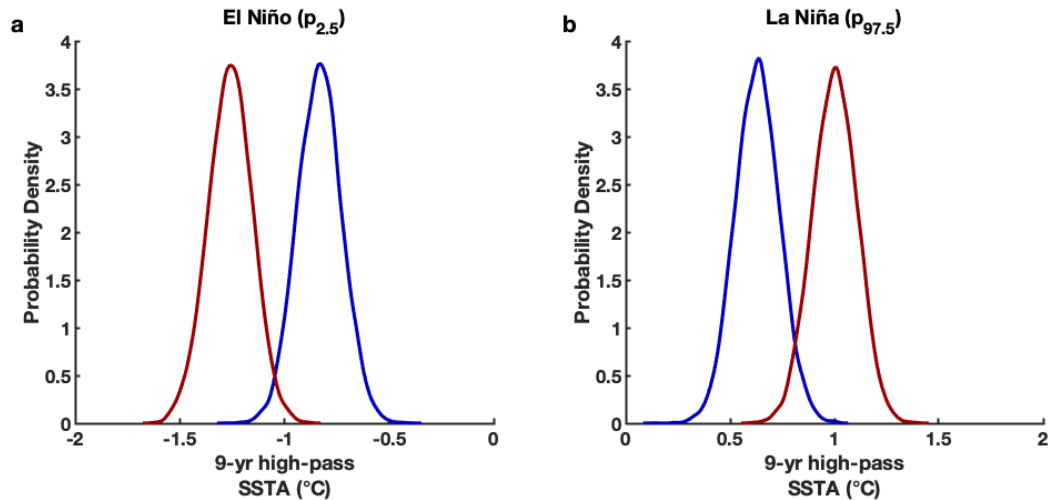
Figure S6. Comparison of Modern (less ENSO variability) and Modern (more ENSO variability) extrema. Gaussian distributions (n = 10,000) of the 2.5 (**a**) and 97.5 (**b**) percentiles for modern SW Pacific coral Sr/Ca-SSTA with their computed uncertainties. PDFs show the overlap between the percentiles in Fig. 7, taking uncertainty into account. **a** El Niño-related SSTA ($p_{2.5}$). **b** La Niña-related SSTA ($p_{97.5}$). PDF for the 20th century interval with more (red: 1980-1999 CE) and less (blue: 1920-1939 CE) ENSO variability (**a**, **b**). The mean percentile values for each PDF in **a**, **b** are from Fig. 7. The $\pm 2\sigma$ uncertainity in the 2.5 and 97.5 percentiles (width of the PDFs) is ± 0.21 °C based on analytical, calibration, and replication uncertainty (Section 3.4). The overlap between the modern (less variable) and modern (more variable) distributions show that the differences in ENSO variability are large outside of the calculated uncertainty.
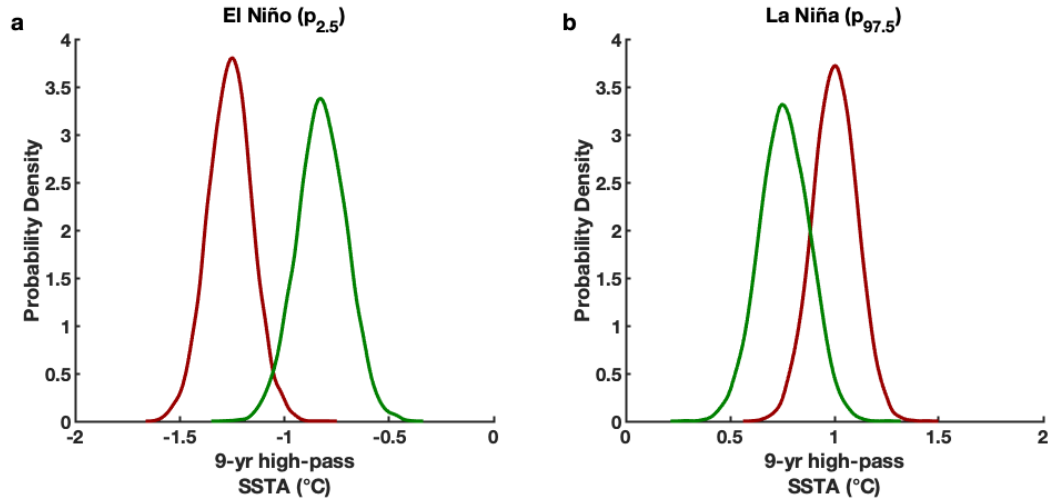
Figure S7. Comparison of Modern (more ENSO variability) and MCA (100 years) extrema. Gaussian distributions (n = 10,000) of the 2.5 (**a**) and 97.5 (**b**) percentiles for the modern interval with more ENSO variability (red: 1980-1999 CE) and the MCA (green: 100 years) based on coral Sr/Ca-SSTA. The mean percentile values for each PDF in **a**, **b** are from Fig. 7. The $\pm2\sigma$ uncertainity in the 2.5 and 97.5 percentiles (width of the PDFs) is ±0.21 °C (modern) and ±0.24 °C (MCA) based on analytical, calibration, and replication uncertainty (Section 3.4). **a** El Niño-related SSTA ($p_{2.5}$). **b** La Niña-related SSTA ($p_{97.5}$). The overlap between the PDFs for the modern (more variable) and MCA is smaller compared to the overlap between the modern (less variable) and the MCA (Supplementary Fig. 5), particularly for El Niño related SSTA (**a**). Incorporating the total uncertainty, ENSO variability during the MCA is different than the interval with more ENSO variability during the late 20th century.
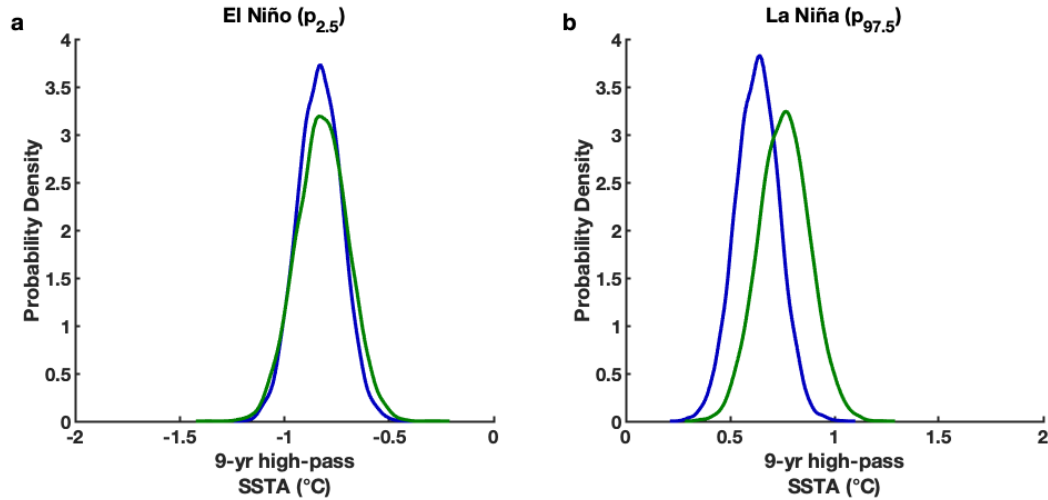
Figure S8. Modern (less ENSO variability) and MCA (100 years) extrema. Gaussian distributions (n = 10,000) of the 2.5 (**a**) and 97.5 (**b**) percentiles for the modern interval with less ENSO variability (blue: 1920-1939 CE) and the MCA (green: 100 years) based on coral Sr/Ca-SSTA. The mean percentile values for each PDF in **a**, **b** are from Fig. 7. The ±2σ uncertainity in the 2.5 and 97.5 percentiles (width of the PDFs) is ±0.21 °C (modern) and ±0.24 °C (MCA) based on analytical, calibration, and replication uncertainty (Section 3.4). **a** El Niño-related SSTA ($p_{2.5}$). **b** La Niña-related SSTA ($p_{97.5}$). Incorporating the total uncertainty in the percentiles, ENSO variability during the MCA is similar to the interval with less ENSO variability during the early 20th century.
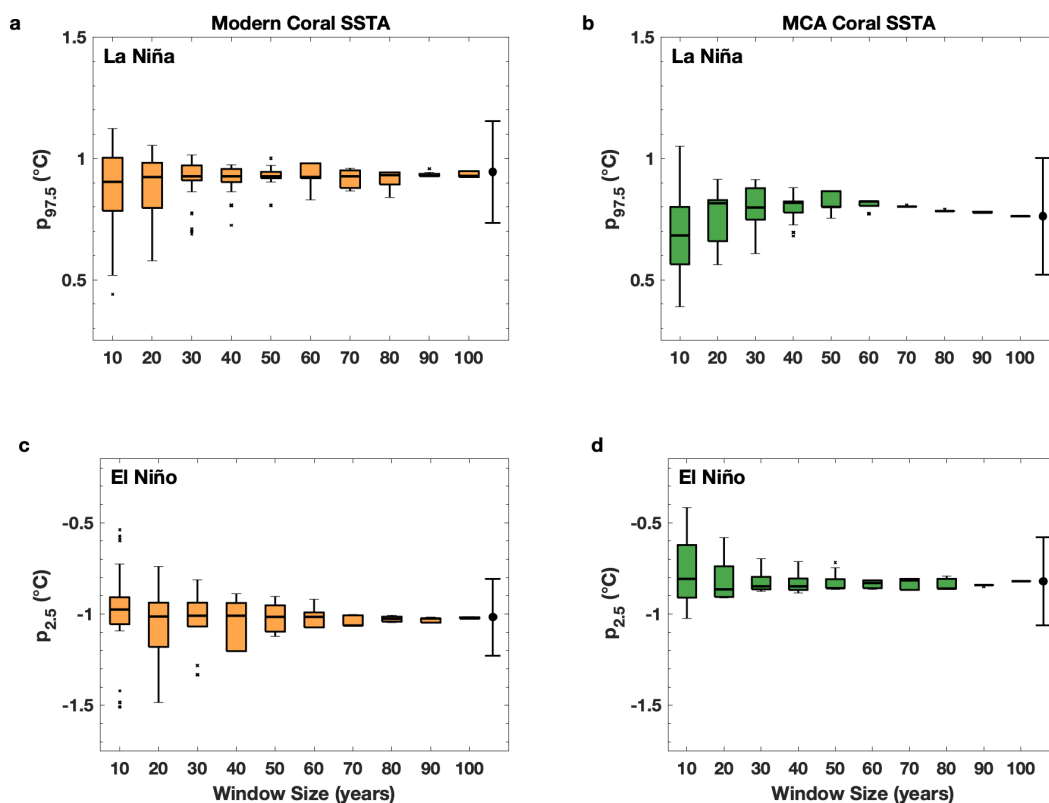
Figure S9. Effect of interval length on variability metrics. a-d Box plots summarizing the 97.5 (**a, b**) and 2.5 (**c, d**) percentile values of reconstructed SSTA computed in sliding windows (x-axis) for the Sabine Bank modern coral (**a, c**), and the Tasmaloum fossil coral 11-TM-S5 (**b, d**). All sliding windows are shifted by 1 year. The lower and upper bounds of the boxes correspond to the 25th and 75th percentiles and the center line indicates the median. The whiskers represent the 1.5 x inter-quartile range (IQR). Values greater than 1.5 x IQR are plotted as outliers (black dots). The median $p_{2.5}$ and $p_{97.5}$ values (horizontal black bar) stays relatively constant as a function of window side, justifying our choice to compare 100 years of MCA data to 20 years of modern data (Fig. 7). The black error bars to the right of the 100-year window in a-d indicate the ±0.21 °C (modern) and ±0.24 °C (MCA) total uncertainty in the SSTA $p_{2.5}$ and $p_{97.5}$ values taking analytical, calibration, and replication uncertainty into account (Section 3.4). The larger the interdecadal changes in ENSO variability due to natural causes, i.e. the 'Wittenberg effect, [*Wittenberg*, 2009]' the larger the size of the box at smaller window sizes.

core name	coral type/species	site name	location	selected coral pieces	total length (cm)	U-Th date ± 2σ (CE)	U-Th date midpoint (cm)	growth rate (avg. ± 2σ, cm/yr)	target temporal resolution	sampling resolution (mm)
06-SB-A1	modern (*P. lutea*)	SBV[a]	15.9 °S, 166.0 °E	a, b, c, d, e(1)	132.5	--	--	1.19 ± 0.19	~monthly	1.0
11-TM-S5[b]	fossil (*P. lutea*)	TMV[c]	15.6 °S, 166.9 °E	a, b, c	114.4	1127.1 ± 2.7	36.4	0.73 ± 0.09	~monthly	0.5, 0.6[d]
11-TM-I1[b]	fossil (*P. lutea*)	TMV[c]	15.6 °S, 166.9 °E	a	62.2	1125.7 ± 6.2	30.5	1.24 ± 0.09	~monthly	0.9
						1142.6 ± 4.9	18.0			
						1149.0 ± 4.1	10.7			

[a] SBV: Sabine Bank, Vanuatu
[b] Fossil coral cores 11-TM-S5 and 11-TM-I1 were collected from the same uplifted reef but different coral heads
[c] TMV: Tasmaloum, Vanuatu
[d] The 11-TM-S5 sampling resolution was adjusted for each piece depending on the average growth rate

Table S1. Coral selection, U-Th dating, and sampling information.

Uranium and Thorium isotopic compositions and ^{230}Th ages for fossil coral 11-TM-S5 by MC-ICP-MS, Thermo Electron Neptune, at NTU.

Sample ID	Depth in core cm	Weight g	^{238}U ppb[a]	^{232}Th ppt	δ^{234}U measured[a]	[^{230}Th/^{238}U] activity[c]	[^{230}Th/^{232}Th] ppm[d]	Age (yr ago) uncorrected	Age (yr ago) corrected[c,e]	$\delta^{234}U_{initial}$ corrected[b]	Year (CE)
11TM-S5b		0.22133	2497.5 ± 2.4	37.2 ± 2.1	143.8 ± 1.4	0.009270 ± 0.000026	10264 ± 580	887.2 ± 2.7	886.9 ± 2.7	144.1 ± 1.4	1127.1 ± 2.7

Notes:

Chemistry was performed in August, 2014 (Shen et al., 2003), and instrumental analysis on MC-ICP-MS (Shen et al., 2012).
Analytical errors are 2σ of the mean.

[a] [^{238}U] = [^{235}U] x 137.77 (±0.11‰) (Hiess et al., 2012); δ^{234}U = ([^{234}U/^{238}U]$_{activity}$ - 1) x 1000.

[b] $\delta^{234}U_{initial}$ corrected was calculated based on ^{230}Th age (T), i.e., $\delta^{234}U_{initial} = \delta^{234}U_{measured}$ X e$^{\lambda 234*T}$, and T is corrected age.

[c] [^{230}Th/^{238}U]$_{activity}$ = 1 - e$^{-\lambda 230 T}$ + ($\delta^{234}U_{measured}/1000$)[$\lambda_{230}/(\lambda_{230} - \lambda_{234})$](1 - e$^{-(\lambda 230 - \lambda 234)T}$), where T is the age.

Decay constants are 9.1705 x 10^{-6} yr^{-1} for ^{230}Th, 2.8221 x 10^{-6} yr^{-1} for ^{234}U (Cheng et al., 2012), and 1.55125 x 10^{-10} yr^{-1} for ^{238}U (Jaffey et al., 1971).

[d] The degree of detrital ^{230}Th contamination is indicated by the [^{230}Th/^{232}Th] atomic ratio instead of the activity ratio.

[e] Age corrections for samples were calculated using an estimated atomic ^{230}Th/^{232}Th ratio of 4 ± 2 ppm (Shen et al., 2008).

Table S2. U-Th information for the ^{230}Th age calculation for fossil coral 11-TM-S5.

Uranium and Thorium isotopic compositions and ^{230}Th ages for fossil coral 11-TM-I1 by MC-ICP-MS, Thermo Electron Neptune, at NTU.

Sample	Depth in core	Weight	^{238}U	^{232}Th	δ^{234}U	$[^{230}$Th/^{238}U]	^{230}Th/^{232}Th	Age (yr ago)	Age (yr ago)	Age (yr BP)	δ^{234}U$_{initial}$	Year (CE)	
ID	cm	g	10^{-6} g/g ^{a}	10^{-12} g/g	measured^a	activity^c	atomic (x 10^{-6})	uncorrected	corrected ^{c,d}	relative to 1950 AD	corrected^b		
11-TM-I1a-1	30.5	0.2540	2.3796 ± 0.0021	28.9 ± 1.8	145.7 ± 1.4	0.009106 ± 0.000041	12371 ± 786	870.0 ± 4.1	869.7 ± 4.1	801.0 ± 4.1	146.0 ± 1.4	1149.0	± 4.1
11-TM-I1a-2	18	0.2680	2.1724 ± 0.0019	14.8 ± 1.7	146.1 ± 1.4	0.009174 ± 0.000049	22263 ± 2615	876.3 ± 4.9	876.1 ± 4.9	807.4 ± 4.9	146.4 ± 1.4	1142.6	± 4.9
11-TM-I1a-3	10.7	0.2375	2.4002 ± 0.0020	17.4 ± 2.0	145.0 ± 1.2	0.009341 ± 0.000064	21199 ± 2381	893.2 ± 6.2	893.0 ± 6.2	824.3 ± 6.2	145.3 ± 1.2	1125.7	± 6.2

Notes:

Analytical errors are 2σ of the mean.

^{a} $[^{238}$U] = $[^{235}$U] x 137.77 (±0.11‰) **(Hiess et al., 2012);** δ^{234}U = $([^{234}$U/^{238}U]$_{activity}$ - 1) x 1000.

^{b} δ^{234}U$_{initial}$ corrected was calculated based on ^{230}Th age (T), i.e., δ^{234}U$_{initial}$ = δ^{234}U$_{measured}$ X e$^{\lambda 234*T}$, and T is corrected age.

^{c} $[^{230}$Th/^{238}U]$_{activity}$ = 1 - e$^{-\lambda 230T}$ + (δ^{234}U$_{measured}$/1000)[λ_{230}/(λ_{230} - λ_{234})](1 - e$^{-(\lambda 230 - \lambda 234)T}$), where T is the age.

Decay constants are 9.1705 x 10^{-6} yr^{-1} for ^{230}Th, 2.8221 x 10^{-6} yr^{-1} for ^{234}U (Cheng et al., 2013), and 1.55125 x 10^{-10} yr^{-1} for ^{238}U (Jaffey et al., 1971).

^{d} Age corrections, relative to chemistry date on September 25th, 2018, were calculated using an estimated atomic ^{230}Th/^{232}Th ratio of 4 (± 2) x 10^{-6} (Shen et al., 2008).

Table S3. U-Th information for the ^{230}Th age calculation for fossil coral 11-TM-I1.

References

Cravatte, S., T. Delcroix, D. Zhang, M. McPhaden, and J. Leloup (2009), Observed freshening and warming of the western Pacific Warm Pool, *Clim Dyn*, *33*(4), 565–589, doi:10.1007/s00382-009-0526-7.

DeLong, K. L., T. M. Quinn, F. W. Taylor, C.-C. Shen, and K. Lin (2013), Improving coral-base paleoclimate reconstructions by replicating 350 years of coral Sr/Ca variations, *Palaeogeogr. Palaeoclimatol. Palaeoecol.*, *373*(C), 6–24, doi:10.1016/j.palaeo.2012.08.019.

Pearson, K. (1920), Notes on the history of correlation, *Biometrika*, *13*(1), 25, doi:10.2307/2331722.

Rayner, N. A., D. E. Parker, E. B. Horton, C. K. Folland, L. V. Alexander, and D. P. Rowell (2003), Global analyses of sea surface temperature, sea ice, and night marine air temperature since the late nineteenth century, *J. Geophys. Res.*, *108*(D14), 14–37, doi:10.1029/2002JD002670.

Wittenberg, A. T. (2009), Are historical records sufficient to constrain ENSO simulations? *Geophys. Res. Lett.*, *36*(12), 3–5, doi:10.1029/2009GL038710.